LArIAT's Muon Range Stack Characterization using Monte Carlo simulation

Ohana Benevides Rodrigues

PHYSICS PH.D. PROGRAM
INSTITUTE OF PHYSICS
FEDERAL UNIVERSITY OF GOIAS

Dissertation presented as a partial fulfillment of the requirements for the degree of

Master in Physics

GOIÂNIA

2018

sibi
sistema de bibliotecas ufg

PRPG
PRÓ-REITORIA DE PÓS-GRADUAÇÃO

UFG

TERMO DE CIÊNCIA E DE AUTORIZAÇÃO PARA DISPONIBILIZAR VERSÕES ELETRÔNICAS DE TESES E DISSERTAÇÕES NA BIBLIOTECA DIGITAL DA UFG

Na qualidade de titular dos direitos de autor, autorizo a Universidade Federal de Goiás (UFG) a disponibilizar, gratuitamente, por meio da Biblioteca Digital de Teses e Dissertações (BDTD/UFG), regulamentada pela Resolução CEPEC nº 832/2007, sem ressarcimento dos direitos autorais, de acordo com a Lei nº 9610/98, o documento conforme permissões assinaladas abaixo, para fins de leitura, impressão e/ou *download*, a título de divulgação da produção científica brasileira, a partir desta data.

1. Identificação do material bibliográfico: **[X] Dissertação** **[ ] Tese**

2. Identificação da Tese ou Dissertação:

Nome completo do autor: Ohana Benevides Rodrigues

Título do trabalho: LArIAT's Muon Range Stack Characterization using Monte Carlo simulation

3. Informações de acesso ao documento:

Concorda com a liberação total do documento [X] SIM [ ] NÃO[1]

Havendo concordância com a disponibilização eletrônica, torna-se imprescindível o envio do(s) arquivo(s) em formato digital PDF da tese ou dissertação.

Ohana B. Rodrigues
Assinatura do(a) autor(a)[2]

Ciente e de acordo:

Ricardo A. Gomes
Assinatura do(a) orientador(a)[2]

Data: 15 / 06 / 2018

---

[1] Neste caso o documento será embargado por até um ano a partir da data de defesa. A extensão deste prazo suscita justificativa junto à coordenação do curso. Os dados do documento não serão disponibilizados durante o período de embargo.

Casos de embargo:
- Solicitação de registro de patente
- Submissão de artigo em revista científica
- Publicação como capítulo de livro
- Publicação da dissertação/tese em livro

[2] A assinatura deve ser escaneada.

Versão atualizada em maio de 2017.

FEDERAL UNIVERSITY OF GOIAS
INSTITUTE OF PHYSICS
PHYSICS PH.D. PROGRAM

Ohana Benevides Rodrigues

LArIAT's Muon Range Stack Characterization using Monte Carlo simulation

Dissertation submitted to the Physics Ph.D. Program of the Institute of Physics at the Federal University of Goias, in partial fulfillment for the degree of Master in Physics, under the advising of Prof. Dr. Ricardo Avelino Gomes.

GOIÂNIA

2018

Ficha de identificação da obra elaborada pelo autor, através do
Programa de Geração Automática do Sistema de Bibliotecas da UFG.

Benevides Rodrigues, Ohana
LArIAT's Muon Range Stack Characterization using Monte Carlo simulation [manuscrito] / Ohana Benevides Rodrigues. - 2018.
xxi, 75 f.: il.

Orientador: Prof. Dr. Ricardo Avelino Gomes.
Dissertação (Mestrado) - Universidade Federal de Goiás, Instituto de Física (IF), Programa de Pós-Graduação em Física, Goiânia, 2018.
Bibliografia. Apêndice.
Inclui siglas, fotografias, abreviaturas, símbolos, gráfico, tabelas, lista de figuras, lista de tabelas.

1. LArIAT. 2. Fermilab. 3. Neutrino. 4. LArTPC. 5. Monte Carlo Simulation . I. Avelino Gomes, Ricardo , orient. II. Título.

CDU 539.12

Universidade Federal de Goiás
Instituto de Física
Programa de Pós-Graduação em Física

Ata **Nº 172** de defesa de dissertação de Ohana Benevides Rodrigues para obtenção do título de Mestre em Física.

Aos 29 dias do mês de junho de 2018, às 14h00min, no Anfiteatro I do Instituto de Física, reuniu-se a Banca Examinadora designada pela Coordenadoria do Programa de Pós-Graduação do Instituto de Física da Universidade Federal de Goiás, composta pelo **Prof. Dr. Ricardo Avelino Gomes** (orientador – IF/UFG), **Prof. Dr. Orlando Luis Goulart Peres** (IFGW/UNICAMP) e **Prof. Dr. Norton Gomes de Almeida** (IF/UFG), para julgar a dissertação de mestrado de **Ohana Benevides Rodrigues**, intitulada: "**LArIAT's Muon Range Stack Characterization using Monte Carlo simulation**". O Presidente abriu os trabalhos agradecendo a presença dos membros da Banca Examinadora e concedeu a palavra a Ohana Benevides Rodrigues, que expôs detalhadamente seu trabalho. Em seguida, os membros da Banca fizeram suas considerações e procederam à arguição do candidato. Concluída essa etapa, a Banca, em sessão fechada, deu prosseguimento ao julgamento do trabalho, atribuindo os seguintes conceitos:

Prof. Dr. Ricardo Avelino Gomes (orientador)	APROVADA
Prof. Dr. Orlando Luis G. Peres (IFGW/UNICAMP)	APROVADA
Prof. Dr. Norton Gomes de Almeida (IF/UFG)	APROVADA

Novamente em sessão aberta, o presidente da Banca anunciou o resultado final do julgamento, declarando o candidato Ohana Benevides Rodrigues APROVADA pela Banca Examinadora. Nada mais havendo a tratar, a sessão foi encerrada e lavrou-se a presente ata que segue assinada pelos membros da Banca Examinadora.

Goiânia, 29 de junho de 2018.

Ricardo Avelino Gomes
Prof. Dr. Ricardo Avelino Gomes (Orientador)

Prof. Dr. Orlando Luis Goulart Peres (IFGW/UNICAMP)

Prof. Dr. Norton Gomes de Almeida (IF/UFG)

Dedicated to my parents and to my fiancée.

Acknowledgements

In between the immense number or people who were part of this, I would like to name a few who gave special contribution.

I would like to thank the LArIAT collaboration for their guidance and patience. But, especially, I would like to thank Gregory Pulliam, Elena Gramellini, Jonathan Asaadi and Jason St. John, who so actively helped me through the production of this piece. I would like to thank my advisor, Professor Ricardo Avelino for providing the opportunity to work on this experiment, and for his patience and time.

To my parents, Andrea de Fátima Benevides and Luis Claudio Rocha Rodrigues, thank you who for working hard to provide me the huge privilege of a higher degree education. To my fiancée, Stefano Tognini, thank you for so tirelessly be by my side during these last few years. To Stefano's parents, Maria da Graça Tognini and Pier Angelo Tognini, thank you for the immense life support you provided me and Stefano during our years living in Goiânia.

To Professor Walter Freeman, thank you for the support provided during the conclusion of this work and for proofreading it. To Patty Whitmore, thank you for the encouragement and for being a good listener during a difficult year.

To all my friends that heard me whine about my master's results over and over again, thanks guys, you are amazing. But especially to Elizabeth Lawson-Keister, Julia Dombroski, Kenneth Ratliff and Merrill Asp, who became my family-by-choice during this past year and kept me going.

And at last, thanks CAPES for the financial support provided during the master's program and thanks NPC fellowship program for giving me the chance to work closely to bright scientists at Fermilab.

“When you’re a kid, they tell you it’s all... grow up. Get a job. Get married. Get a house. Have a kid, and that’s it. But the truth is, the world is so much stranger than that. It’s so much darker. And so much madder. And so much better.”

Elton Pope

Abstract

Liquid Argon Time Projection Chambers (LArTPCs) are ideal detectors for precision neutrino physics, but their technology is not completely mastered so far. In order to achieve a complete domain over the technology, the Liquid Argon In A Testbeam (LArIAT) experiment was built. LArIAT consists of a LArTPC placed at a dedicated calibration test beamline at Fermilab. In 2016 LArIAT performed the first pion-argon cross section measurement in history. The Aerogel Cherenkov detectors and the Muon Range Stack (MuRS) detector are auxiliary detectors whose purpose is to separate incoming pions and muons at the Time Projection Chamber (TPC) and separate the through-going muons and pions from the TPC, respectively. These detectors' data were not used on this first analysis due to the lack of people working on their data reconstruction. Therefore, on this work we used as tool the Geant4 Monte Carlo software to characterize the MuRS detector and quantify its purity and efficiency on muon/pion separation.

Resumo

Câmaras de projeção temporal de argônio líquido (do inglês, LArTPC), são detectores considerados ideais para a física de neutrinos de alta precisão por permitirem a reconstrução de trajetórias de partículas com precisão na ordem de milímetros. Apesar de seu potencial, a tecnologia ainda não é perfeitamente dominada. Com este objetivo em mente, o experimento Liquid Argon In A Testbeam (LArIAT) foi construído. O LArIAT consiste em uma câmara de projeção temporal colocada em uma linha de feixe dedicada. Em 2016, o LArIAT apresentou a primeira medida de seção de choque entre píons e argônio líquido da história. Na ocasião da publicação deste resultado, dois dos detectores acessórios do experimento ainda não tinham seus dados reconstruídos: o detector Cherenkov de aerogel e o Muon Range Stack (MuRS). O último é o foco deste trabalho. O objetivo fundamental do MuRS é permitir a distinção entre píons e múons cujas trajetórias não estão completamente contidas dentro do LArTPC. Para investigar a capacidade do detector de distinguir múons e píons e quantificar sua eficiência e pureza, este trabalho simulou a interação de píons e múons com o detector via Monte Carlo utilizando o Geant4.

Contents

List of Figures

List of Tables

Chapter 1

Introduction

Liquid Argon Time Projection Chambers (LArTPCs) are tracking calorimeters with high granularity, providing track resolution at the mm scale. As such, the technology is being applied in the next generation of detectors used in neutrino physics to study both beam and atmospheric neutrinos, as well as searching for proton decay. The United States neutrino program is based on this technology, funding a wide range of detectors for both long and short baseline studies. In order to reach the desired scientific goals set by the program, this technology must be completely developed and understood. Pursuing that, the Liquid Argon In A Testbeam (LArIAT) experiment was proposed.

The LArIAT experiment consists of a LArTPC placed in a dedicated calibration test beamline at the Fermi National Accelerator Laboratory (Fermilab). A set of accessory detectors for particle identification are part of the experiment apparatus and are used to identify particles' mass, charge, and momenta prior to their entrance in the LArTPC, so that the particle interaction with the detector can be fully understood. LArIAT ran successfully during three data-taking runs of roughly 6 months each. The data from the first run was partially analyzed and produced the first pion-argon cross-section in history.

The pion cross-section analyses did not consider the data collected from two detectors, the aerogel Cherenkov detectors and the Muon Range Stack (MuRS) detector, due to lack of reconstruction information from their data. The first of these is placed prior to the LArTPC cryostat, and the latter being located after it. Currently, the estimated through-going muon contamination on the pion data is equal to 3%, and the aim of those two accessory detectors is to reduce it. The contamination is caused by the misidentification of pions and muons due to their similar calorimetric energy loss and due to the fact that they are not-fully-contained within the LArTPC. These non fully contained events will reach the MuRS detector, which is expected to identify pions from muons.

The goal of this work is to characterize and validate the Muon Range Stack Detector using a Monte Carlo simulation. This analysis provides a better understanding of the efficiency of the detector in separating pions from muons, and allows us to optimize its usage. To do so, this study is presented in the following order:

Chapter 2 provides an overview of the LArTPC technology, as well as current and future LArTPC experiments.

Chapter 3 describes the motivation and the goals of the LArIAT experiment.

Chapter 4 describes the full LArIAT experimental apparatus, along with a more in-depth description of the MuRS detector, as it is the focus of this study.

Chapter 5 describes the Monte Carlo simulation, its analysis, and presents the results.

Chapter 6 outlines the conclusions of this study.

Chapter 2

Prospective LArTPC-Based Neutrino Experiments

2.1 LArTPCs overview

Time Projection Chambers (TPCs) are a type of particle detector first proposed by David Nygren in 1974 [1]. It consists of a volume filled with a sensitive gas or liquid in a strong ($\sim$500 V/cm) electric field. When a charged particle passes through the active volume of the detector, the material is ionized, leaving behind a track of ionization charge. The electric field causes this ionization charge to drift towards the wire planes, where sensitive electronics will record the inductive signal and current (see figure 2.1). Using a two (or more) plane setup, with at least one being an induction plane and the other being a collection plane, and a light trigger to calculate the drift time, it is possible to produce a three dimensional calorimetric reconstruction of the track (see figure 2.2).

In 1977, Carlo Rubbia proposed the use of liquid argon as the sensitive material for TPCs [3], a concept that was later implemented by The Imaging Cosmic and Rare Underground Signals (ICARUS) collaboration [4]. There are many good reasons to use liquid argon on TPCs: *i)* it is dense (1.4 g/cm^3), which increases the interaction probability; *ii)* it does not attach electrons, allowing long drift distances, which allows the construction of big detectors; *iii)* it has a high electron mobility; *iv)* argon is the third most abundant gas in the atmosphere, easy to obtain and purify, and thus relatively cheap; *v)* it is inert and can be liquified with liquid nitrogen [3]. To guarantee the second and third points, the purity of the liquid argon is fundamental and, therefore, contaminants such as water and oxygen should be minimized as low as 0.1 parts per billion (ppb) [5]. Due to all those characteristics, and the capability to deliver the advantages of bubble chambers and electronic detectors, LArTPCs became one of the most promising technologies for future large scale neutrino detectors.

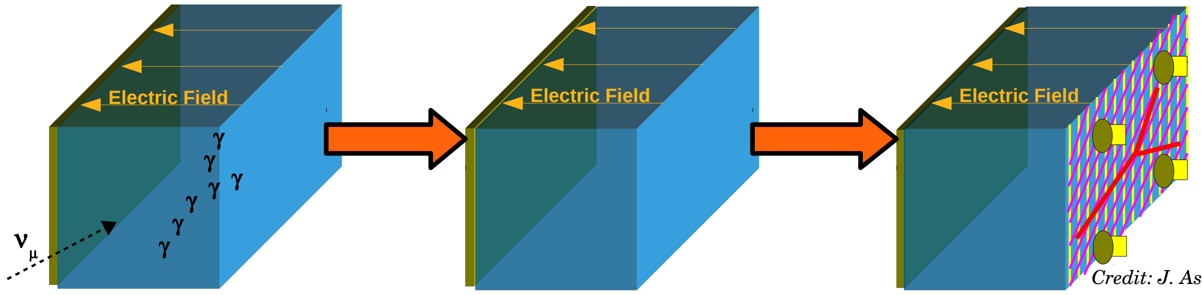

Credit: J. Asaadi

Neutrino interaction in LAr produces ionization and scintillation light

Drift the ionization charge in a uniform electric field

Read out charge and light produced using precision wires and PMT's

Figure 2.1 | LArTPC detection steps
The figure shows in steps how a LArTPC works. When a particle passes through its fiducial volume and interacts with the Liquid Argon (LAr), ionization charges and scintillation light are produced. The electric field causes the produced ionization charges to drift through the detector until they reach the collection plane. Charge and light are read by precision wires and photomultipliers (PMTs), respectively [2].

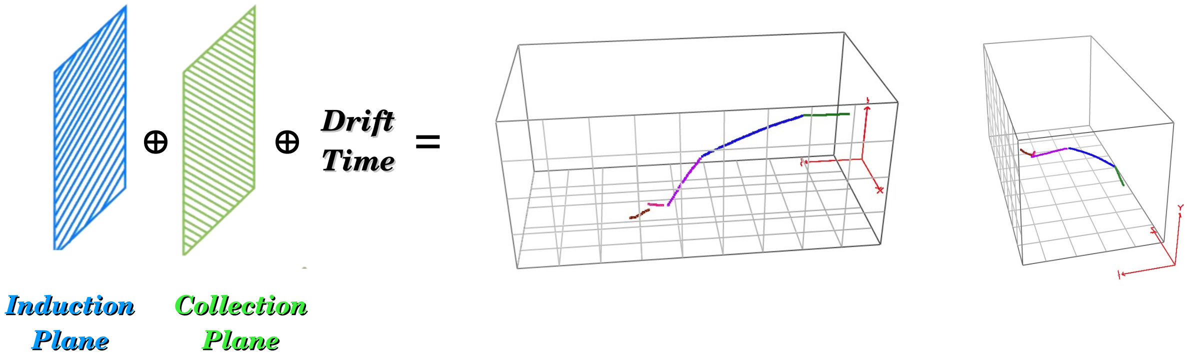

Figure 2.2 | LArTPC read out system
The figure shows the basic composition of the LArTPC read out system. The mini@s mum setup includes one induction wire plane, one collection wire plane, and a set of PMTs. The information retrieved by those 3 components allows 3D track reconstruction [2].

2.2 Short Baseline Experiments

2.2.1 MicroBooNE

The Micro Booster Neutrino Experiment (MicroBooNE) is a LArTPC of 90 tons lying inside a cryostat that carries 170 tons of liquid argon when full. The detector consists of two main components: *i)* three readout planes, and *ii)* 32 photomultipliers plus four light guide paddles, all built in one single containment vessel (see figure 2.3). The readout planes encompass two induction planes at ±60° with respect to vertical and one collector plane at vertical, all with a 3 mm wire pitch, while the latter component is necessary for determining the starting time of the recorded events. MicroBooNE is located at Fermilab, next to the MiniBooNE detector[1] hall and is exposed to the on-axis Booster Neutrino Beam[2] as well as an off-axis component of the Neutrinos at the Main Injector (NuMI) beam. MicroBooNE's main goals can be summarized as:

i) expand the resolution of the MiniBooNE low energy excess [8, 9],

ii) perform measurements of neutrino cross-section, and

iii) understand low energy (below 475 MeV) neutrino interactions.

MicroBooNE, as a LArTPC, is the ideal detector to achieve good resolution in low energy events by its good e/γ separation capability [10].

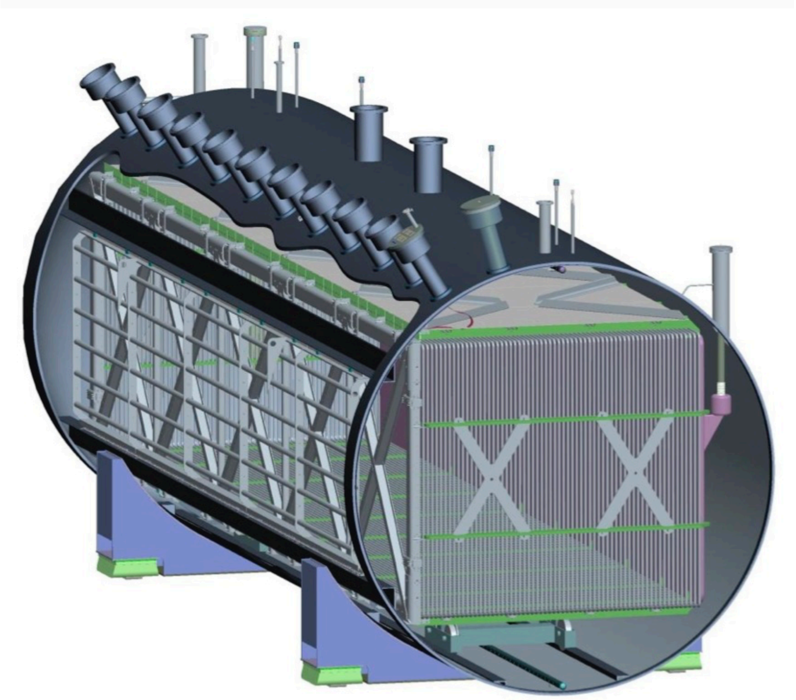

Figure 2.3 | MicroBooNE's detector
MicroBooNE's detector design [11].

---

[1] The Mini Booster Neutrino Experiment (MiniBooNE) experiment at Fermilab built to look for $\nu_\mu \longrightarrow \nu_e$ oscillations and started collecting data in 2002 [6].

[2] The Fermilab Booster is a synchrotron accelerator. It provides, among many other lines, 8 GeV protons to the MiniBooNE target hall which contains a beryllium target. The collision of the protons on the beryllium target produces a neutrino beam [6, 28].

2.2.2 ICARUS

The Imaging Cosmic and Rare Underground Signals (ICARUS)[3] is an experiment that is currently being installed at Fermilab, where it will operate in a short baseline distance as a complementary to the MicroBooNE experiment. The experiment consists of two detectors, namely the T600 and the T150. The T600 detector is made of a large cryostat filled with a total of 760 tons of argon weight (~ 476 tons active). The readout planes encompass 2 induction planes at $\pm 60^\circ$ with respect to horizontal and 1 collector plane at horizontal, all with a 3 mm wire pitch. The T150 detector is functionally identical to the T600, but scaled down to 25% of its size. The T600 detector will be located along the Booster Neutrino Beamline (BNB) at an approximate distance of about 700 m from the target, while the latter will be located at about 150 m from the target (see figure 2.4). The light collection system to be used is still under scrutiny [13].

Due to its reduced mass, MicroBooNE is limited to the study of neutrinos, as the antineutrino signal is too weak for a sensitive comparison. With the addition of the ICARUS detector at Fermilab, said weakness is compensated by the larger mass of the T600 detector. Another positive aspect of two functionally identical detectors located at different positions at Fermilab is the fact that both should have experimentally identical signatures of neutrino oscillations, allowing analyzes without any need of Monte Carlo comparisons [13].

---

[3] From 2010 to 2014, ICARUS was managed by the Italian Institute for Nuclear Physics (INFN), at the National Laboratories of the Gran Sasso (LNGS). By that time, ICARUS used as a primary neutrino source the CERN Neutrinos to Gran Sasso (CNGS) neutrino beam, located at the European Council for Nuclear Research (CERN), which crosses 730 km of the Earth's crust while traveling from CERN to INFN, being considered a long baseline experiment. Despite the fact that the main source of neutrinos was a high intensity beam, the experiment also analyzed atmospheric neutrinos. At the end, a total of about 3000 neutrino beam events were successfully collected, which allowed ICARUS to produce many interesting results. Concerning physics results, it is important to highlight the "Precision measurement of the neutrino velocity with the ICARUS detector in the CNGS beam" [12]. Related to the technical ones, there were verifications of the detector performance and validation of the simulation packages, as well as progresses in event reconstruction algorithms.

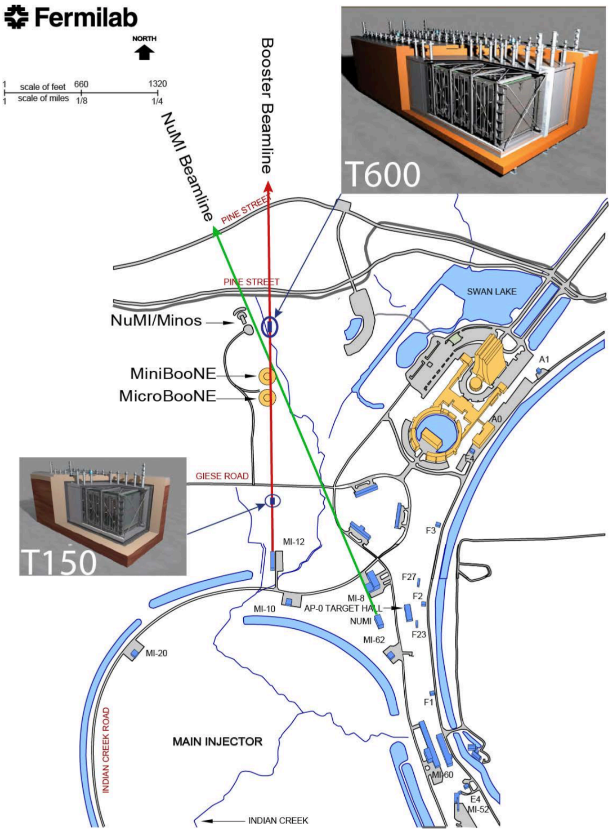

Figure 2.4 | ICARUS at FNAL
The figure shows a layout of the FNAL Booster neutrino beam line and where the T600 and T150 detectors will be placed [13].

2.2.3 Short-Baseline Near Detector (SBND)

The SBND experiment is a 112 ton active volume LArTPC (220 ton in total) (see figure 2.5) located at Fermilab, placed only 110 m from the Booster Neutrino Beam. The detector is currently in the design phase and it is expected to begin operation in 2018. Details on the positioning of the wire planes and light collection system are under discussion.

By detecting millions of un-oscillated neutrino interactions per year, SBND will be crucial to perform searches for neutrino oscillations at the Fermilab Short-Baseline Program.

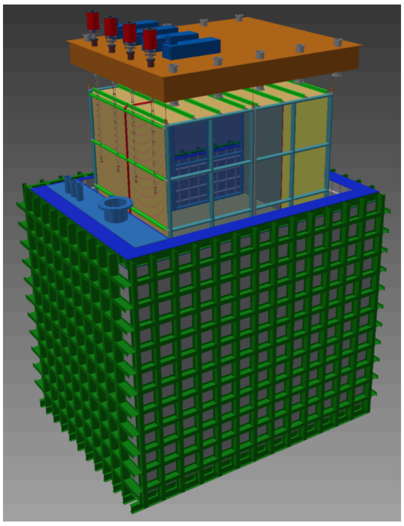

Figure 2.5 | SBND Detector
The SBND schematic drawing [14].

2.3 Long Baseline Experiments

2.3.1 DUNE

The Deep Underground Neutrino Experiment (DUNE) is by far the most promising experiment for neutrino physics. It is planned to be fully operating by 2026, and will be composed of two detectors: a Near Detector at Fermilab and a Far Detector, 1,300 km away and placed in a depth of $\sim 1{,}500$ km, at the Sanford Underground Research Facility, located in South Dakota (see figure 2.6). DUNE will have a massive modular LArTPC, with four modules, each containing around 10 kton of fiducial mass (see figure 2.7). DUNE's goal is to address a number of the fundamental open questions in particle and astroparticle physics. Among those questions, DUNE will address: Measure the CP violating phase in the leptonic sector; determine the character of the neutrino mass spectrum; make precision measurements of oscillation parameters; search for baryon number violating processes (nucleon decay), and precision measurements of neutrinos from a core-collapse supernova within the Galaxy [15]. For a comprehensive description on neutrino physics, its challenges, and open questions, see Appendix A. DUNE's source of neutrinos will be a new Fermilab's neutrino beamline with a power of up to 1.2 MW (until 2026), with a planned upgrade to reach up to 2.4 MW by 2030. To control the systematic uncertainties, DUNE's Near Detector will be extremely precise and will include argon targets to measure the absolute flux and energy of all the neutrino species. To be able to separate between fluxes of neutrinos and antineutrinos, the Near Detector will be magnetized, so it can charge-discriminate electrons and muons produced in the neutrino interaction. DUNE's Near Detector design will be similar to the Neutrino Oscillation Magnetic Detector's (NOMAD) experiment at CERN (see 2.8) [16].

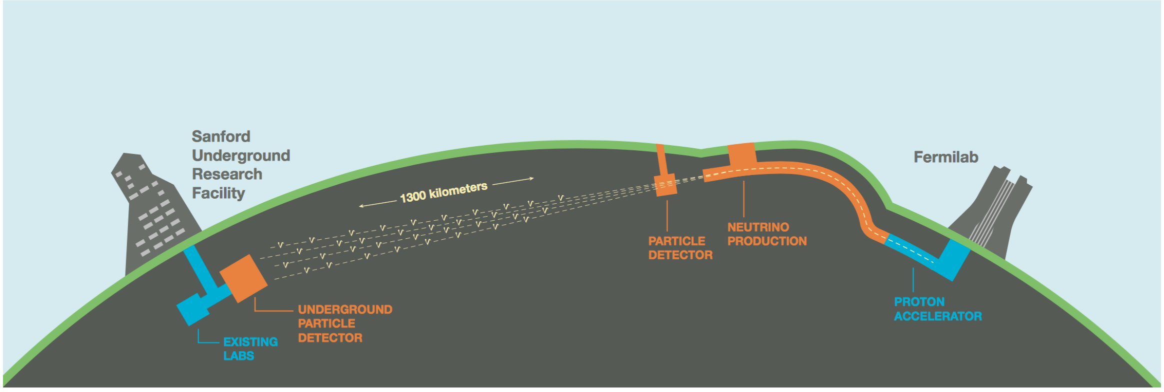

Figure 2.6 | DUNE’s full schematic.
The figure shows the full DUNE’s schematics, providing a view of the production of the neutrino beam, the Near Detector at Fermilab, the under crust travel of the beam, and the Far Detector at SURF [15].

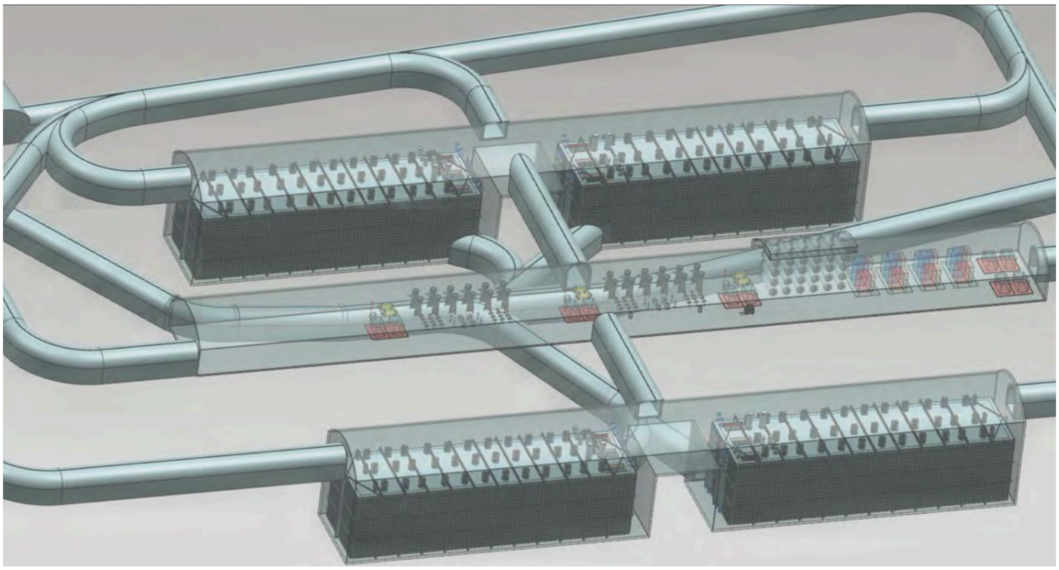

Figure 2.7 | DUNE’s Far Detector underground cavern layout.
The figure shows the isometric view of DUNE’s Far Detector underground cavern layout, with the four 10 kton modules. [17].

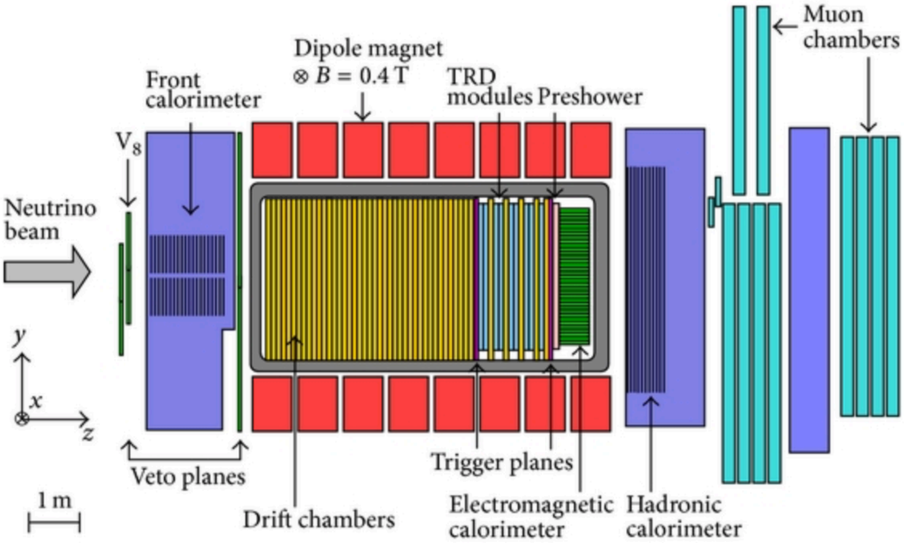

Figure 2.8 | NOMAD's experiment drift chamber.
The figure shows the side view of NOMAD's drift chamber [16].

Chapter 3

The LArIAT Experiment

3.1 Motivation for a Liquid Argon In A Testbeam Experiment

The very high granularity provided by the LArTPC technology makes this type of the detector the best choice for precision neutrino physics and, when located deep underground, experiments have the capability to measure astrophysical neutrinos and to search for proton decay. As a new technology, there is the fundamental need to stress test it and fully understand its response to particle passage. As such, one of the most important steps to fully understand the technology is to understand the exact signals that the interesting particles in the relevant energy ranges will leave in the detector [18]. In this scenario, the Liquid Argon In A Testbeam Experiment (LArIAT) is an experiment that consists of placing a LArTPC in a dedicated calibration test beamline at Fermilab. By controlling the particles produced in the beamline and their energies, and by placing accessory detectors prior to the TPC, it is possible to know beforehand the mass, momentum, and charge of the particles that are entering the LArTPC, allowing the study of the signal measured by the LArTPC. The experimental knowledge gathered by LArIAT will provide precious information for the future neutrino experiments, contributing to the success of the future of neutrino physics.

3.2 LArIAT's Main Goals

3.2.1 e to γ-initiated Shower Separation

Weak interactions can occur via charged-current (CC) or via neutral-current (NC). In CC ν_e interactions, the final product can be a positron or an electron. Alternatively, in NC interactions, the result often is a π^0 that promptly decays into two photons, each of which can pair-produce to form electromagnetic showers. In this context, one of the most interesting features that LArTPCs provide to neutrino physics is the capacity to distinguishing electron showers from γ

showers. Given the fact that no experimental measurement of the efficiency of this technique was ever done, one of LArIAT's goals is to evaluate it [19]. Figure 3.1 shows how the signals of both electron and photon-initiated showers candidates will be visualized by the LArIAT event display.

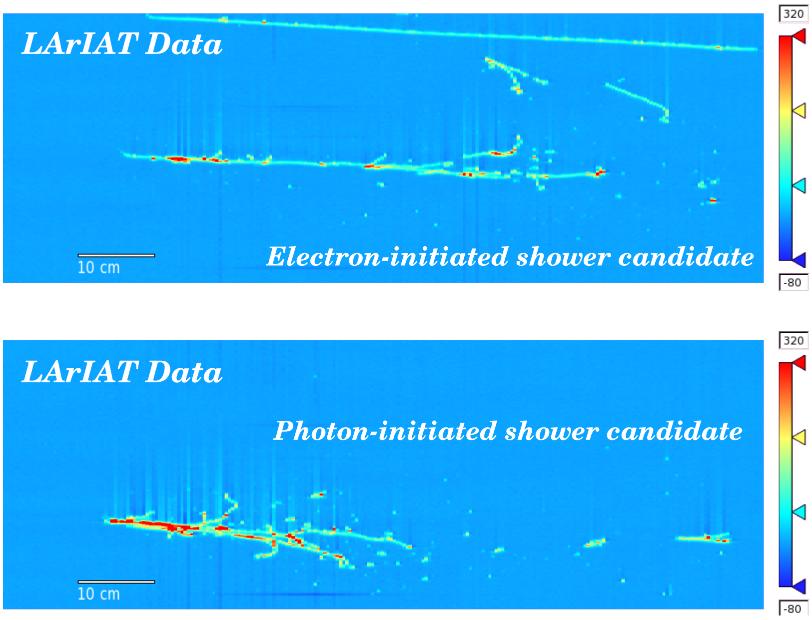

Figure 3.1 | Electron and photon initiated shower candidates
LArIAT event display images of electron-initiated shower candidate (top) and photon-initiated shower candidate (bottom) [20].

3.2.2 Charge Sign Determination

Some particles can have their sign identified based only on topological criteria. For example, positive stopping muons only interact by decay, with the emission of a positron with a determined energy spectrum. Negative stopping muons can either decay with the emission of an electron or be captured by nuclei. Argon nuclei capture negative muons in 76% of the cases, producing a neutron and a photon in the process. Thus, it is possible to identify the decay of positive muons over the negative muon capture by a nucleus via the detection of a delayed Michel electron track in the LArTPC (see figure 3.2). Albeit conceptually well understood, a systematic analysis of the processes following the negative muon capture by argon was never carried forward and, consequently, LArTPCs true capability to topologically identify particle charge is yet to be known.

LArIAT's switching polarity capability and beamline detectors provide the possibility to determine the efficiency and purity of charge separation for pions, muons, and kaons. The capacity to distinguish the sign of the decay and capture products allows the identification of

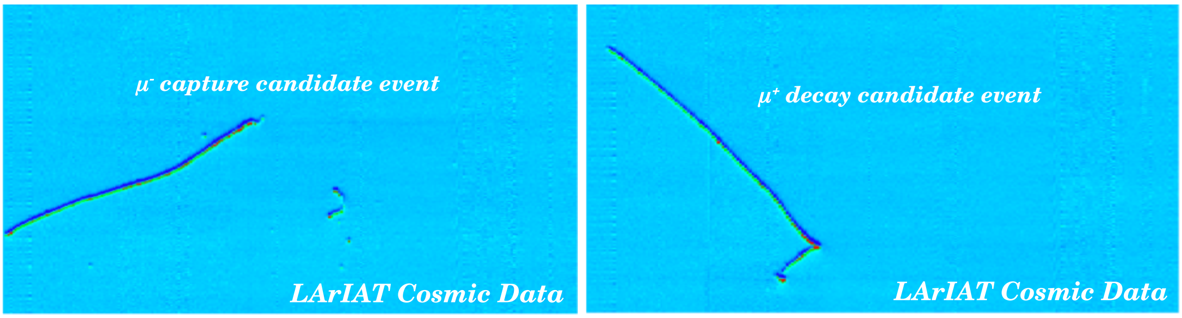

Figure 3.2 | μ^- capture candidate and μ^+ decay candidate
LArIAT event display images of a μ^- capture candidate and a μ^+ decay candidate [20].

the charge of the primary lepton in ν_μ CC interactions, which is particularly important for CP violation measurements [18].

3.2.3 Single Track Calibration

The calibration of liquid argon detectors consists of determining the relationship between the collected ionization charge and the energy deposited in liquid argon by incident particles of different stopping powers. More specifically, measurements of electron-ion recombination in liquid argon are a key feature to the full comprehension of the technology. Until now, the recombination measurements were sparse. ICARUS had some few measurements in the 15 – 20 kV/cm electric field range, and ArgoNeuT[1] performed some measurements with constant electric field. As such, a study evaluating the relation of recombination within an extended range of energy deposition rates, with electric field values in the typical 0.3 to 1.0 kV/cm, and different angles of incidence of particles with respect to the electric field is essential to understand the fundamental properties of liquid argon and the calorimetric resolution of the detector. A better understanding of these properties will improve the reconstruction and simulation models developed in LArSoft[2] [18]. Given the pure low momentum beams that LArIAT has access to, and the LArTPC high calorimetric resolution that allows the identification of individual tracks, LArIAT has all the necessary apparatus to perform such needed studies.

3.2.4 Pion Interactions in Argon

Neutrino interactions with the nucleus are mediated by the exchange of W or Z bosons. Typically, the exchanged boson interacts with a bound nucleon, increasing its Fermi momentum within the nucleus and producing an outgoing nucleon or, in cases where the incoming neutrino

---

[1] The Argon Neutrino Teststand (ArgoNeuT) detector operated at Fermilab from September 2009 to February 2010. It consisted of a 170 L LArTPC placed upstream of the MINOS Near Detector, with the NuMI beam being ArgoNeuT's neutrino source. The experiment detected neutrinos in the 0.1 to 10 GeV range, providing the first measurement of a LArTPC performance for detecting low energy neutrinos [21].

[2] The Liquid Argon Software (LArSoft) is the framework developed by Fermilab to perform data analysis in LArIAT and other liquid argon based experiments.

is energetic enough (∼GeV), hadrons – with pions being the common hadrons produced (see figure 3.3) [22].

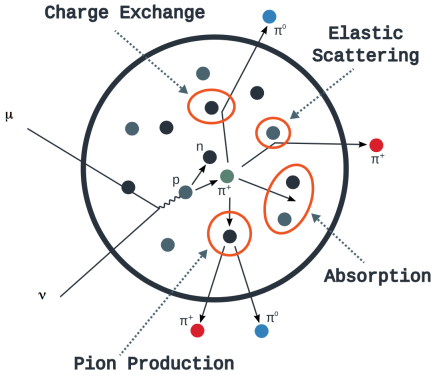

Figure 3.3 | Pion production in neutrino-nucleus interaction
Schematic of pion production in a neutrino-nucleus interaction [22].

The lack of knowledge of pion-nucleus interaction cross-sections is a major source of systematic uncertainty in precision neutrino oscillation physics experiments. As a specific example, a pion single charge exchange reaction can mimic the signature of a NC-ν event, showing that systematic studies such as this case are extremely important. In this scenario, LArIAT is capable of measuring pion-argon cross-sections, as well as some of its contributing components (elastic and inelastic scattering, absorption, charge exchange, secondary pion production), what reduce systematic uncertainties for future neutrino experiments. Figures 3.4 and 3.5 show LArIAT event display images of an absorption event candidate and a charge exchange event candidate, respectively.

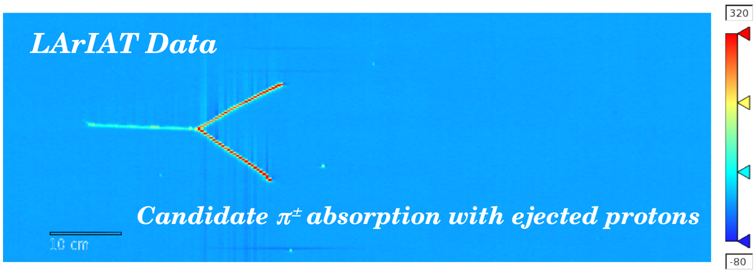

Figure 3.4 | Charged pion absorption
LArIAT's event display image of a charged pion absorption event [20].

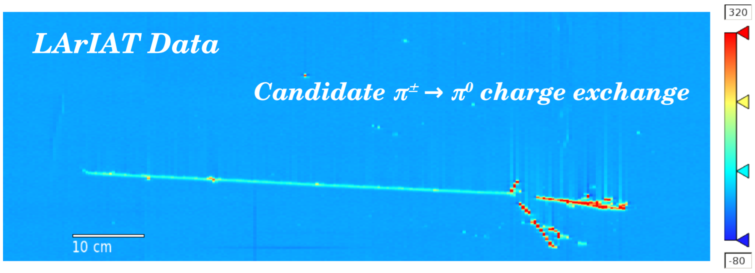

Figure 3.5 | Pion charge exchange
LArIAT's event display image of a pion charge exchange event [20].

All knowledge that LArIAT accumulates on the pion-argon cross section will help develop pion identification algorithms based on their interaction modes in argon [19], which is of great relevance for future experiments.

3.2.5 Kaon Interactions in Argon

One of the goals of the DUNE Experiment is to search for proton decay. Such studies can only be achieved due to the fact that liquid argon imaging capabilities are especially suitable for proton multi-prong decay modes. Many of these channel modes involve protons decaying into kaons and, therefore, require high efficiency in kaon detection. In order to carry forward such studies, it is necessary to conduct a systematic study of kaon interactions and identification in LAr, which is one of LArIAT's main goals [18, 19, 23]. Figure 3.7 shows a LArIAT event display image of a kaon decay candidate.

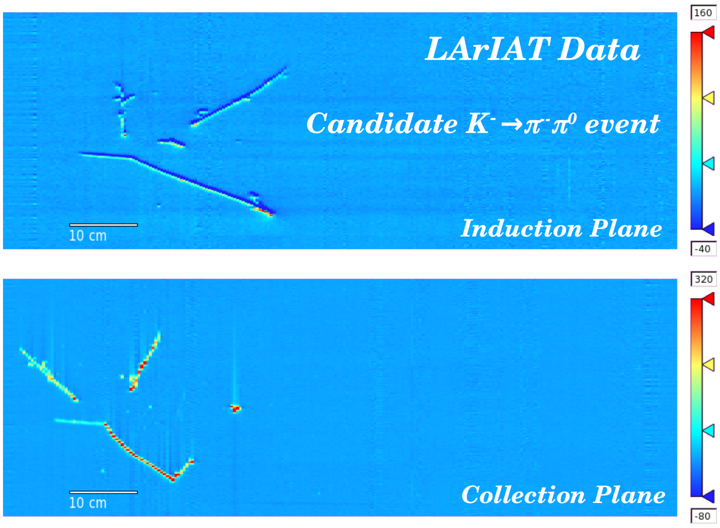

Figure 3.6 | Kaon decay candidate
LArIAT's event display image of a candidate event of a kaon decaying into a π^+ and a π^0. Both induction plane (top) and collection plane (bottom) views are showed [20].

3.2.6 Particle Identification

Efficient particle identification in LArTPC detectors is another essential aspect for the success of the prospective LArTPC-based neutrino experiments. Better particle identification results in a higher confidence level when separating signal from background in neutrino cross-section studies [18]. In LArIAT, the particle identification is performed by the Particle Identification Algorithm (PIDA), originally developed by ArgoNeuT. This method is applied to stopping particles only (i.e. low momentum values), so their energy range is applicable to the power law dependence of the Bethe-Bloch equation. In this method, the first step calculates the energy lost by the particle by multiplying the stopping power provided by the Bethe-Bloch equation and the step length (dX), which returns the total energy loss on said dX. The second step calculates the current kinetic energy of the particle after its energy loss while traversing one unit of step length, and is written as:

$$E_K^{(1)} = E_K^{(0)} - \frac{dE}{dX} dX, \tag{3.1}$$

where $E_K^{(1)}$ is the kinetic energy of the particle after one step length, $E_K^{(0)}$ is the starting kinetic energy of the particle, and $\frac{dE}{dX} dX$ is the energy lost by the particle. The iteration continues until the energy lost in a said step is higher than the kinetic energy of the particle in the previous step (i.e. after said step, the particle would no longer have kinetic energy).

An easy way of representing the stopping power formula is by parameterizing it as a function of a residual range R, which is the distance between a given point of the idealized trajectory and the measured stopping point, and two free parameters, namely A and b:

$$\left(\frac{dE}{dX}\right)_{\text{hyp}} = AR^b. \tag{3.2}$$

The integration of the equation above provides the parametric function for the kinetic energy of a particle

$$E_K = \frac{A}{b+1}R^{b+1}. \tag{3.3}$$

It is known that all particles of interest in LArIAT have similar values of the parameter b [24], as presented in table 3.1, which shows very little variation in b for different particles. As such, the PIDA method relies on fixing a standard value for $b = -0.42$ and measuring the parameter A for a said particle that is traversing the detector. This is accomplished by measuring the (dE/dX) in each space point i of the detector and estimating its parameter A from equation 3.2:

$$A_i = \left(\frac{dE}{dX}\right)_i R_i^{0.42}. \tag{3.4}$$

A final A value is calculated by averaging all A_i of all spatial points and comparing it to the expected A value for each particle, allowing the identification of the particle species. The error introduced in the calculation of A due to the fixed b value is smaller than the error caused by ionization fluctuations [24].

Particle	**A (MeV/cm^{1-b})**	**b**
Pion	8	-0.37
Kaon	14	-0.41
Proton	17	-0.42
Deuteron	25	-0.43

Table 3.1 | Stopping power parameterization
Stopping power parameterization for various particle types in argon at a density of 1.38 g/cm^3. [24].

In 2013 ArgoNeuT simulated muons, pions, kaons, and protons using Geant4 [25], and applied the PIDA method to each particle. The results can be seen in figure 3.8.

3.2.7 Anti-Proton Stars in LAr

Model predictions of anti-proton annihilation (see figure 3.9) vary widely, so it is important for experiments to validate them. As hadron stars' multiplicity is considered very relevant for $n\overline{n}$ oscillation searches, and given that LArIAT's beamline provides low momentum $\overline{p}$, the

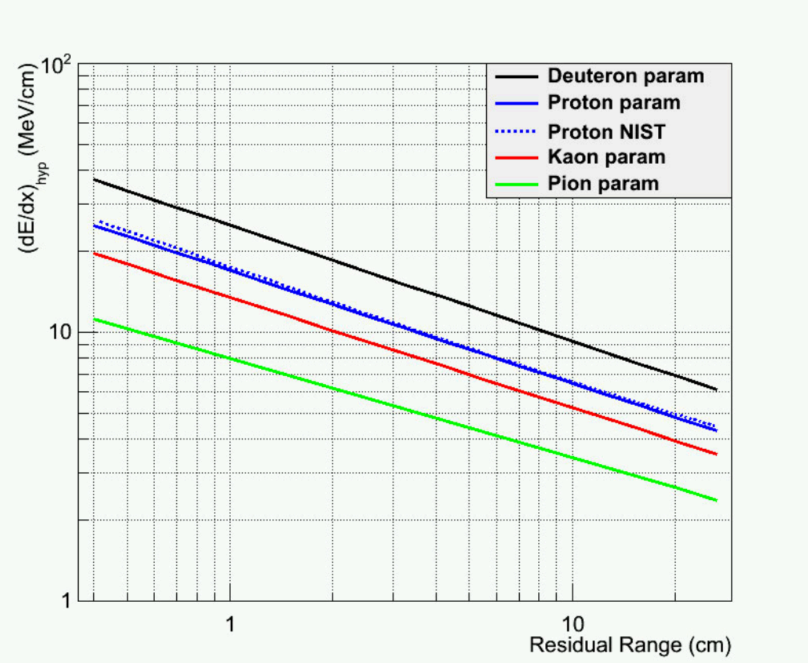

Figure 3.7 | Parameterized stopping power
Parameterized stopping power for various particles as a function of residual range (solid lines). The blue dotted curve shows the NIST stopping power for protons in argon at a density of 1.383 g/cm^3 [24].

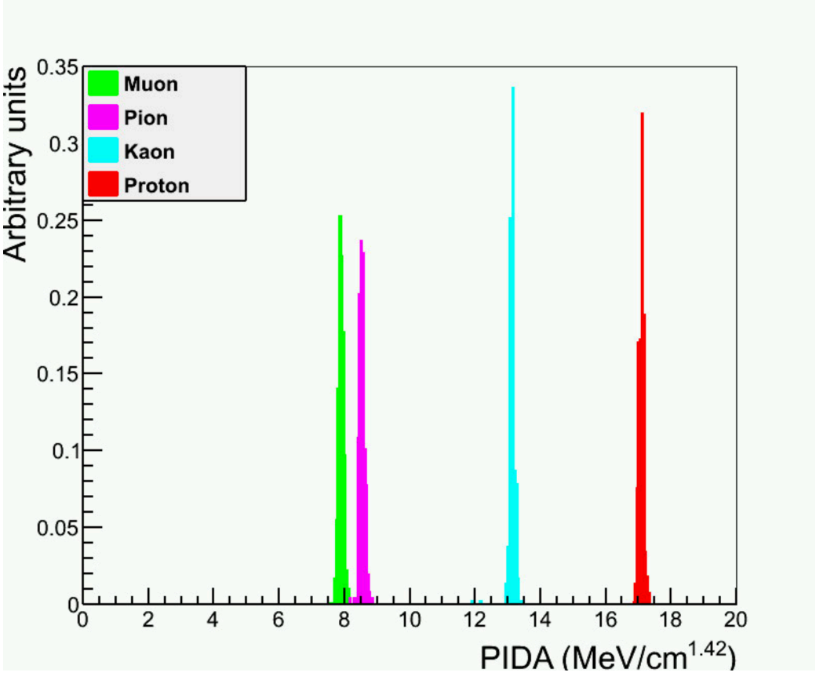

Figure 3.8 | PIDA distribution for MC
PIDA distribution for Monte Carlo generated muons, pions, kaons, and protons using true information [24].

experiment allows the first study of hadron star topology from $\overline{p}p$ annihilation at rest in argon through the proton-argon reaction [18], with results being useful for future neutrino studies.

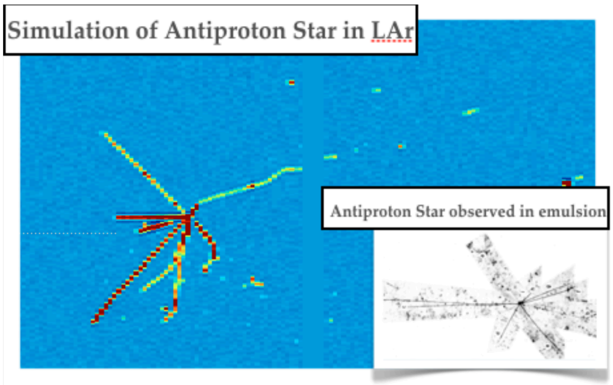

Figure 3.9 | Simulation of an anti-proton star in LAr
Image of the simulation of an anti-proton star in LAr. In the inset, an image of an anti-proton star observed in emulsion [18].

Chapter 4

LArIAT's Experimental Apparatus

4.1 Beamline

4.1.1 Primary Beam

At the beginning of the accelerator chain (see Fermilab's full beam chain in 4.1), there is an hydrogen container. A molybdenum cathode is installed inside the container in the ion source machine. Then the molybdenum's electrons are excited and collected by the hydrogen atoms. The result is an H$^-$ gas. An "extractor" attracts the negative particles with a positive potential, pulling them through a hole with a width of a few mm, while a magnetic field guides them in the right direction in order to feed the beam into a radio-frequency quadrupole (RFQ). The RFQ accepts low-energy beam from the ion source at one end, accelerates the beam up to 750 keV [26], and injects it into the Linear Accelerator (LINAC). The LINAC has a total length of 150 m and is divided in two acceleration parts. The first is a drift tube that accelerates the beam up to 116 MeV, while the second part is a side-coupled cavity that accelerates the beam up to 401 MeV [27]. Exiting the LINAC, the beam collides with a thin carbon sheet. This process removes electrons from the H$^-$, resulting in three beams: an H^- beam, an H^+ beam, and a neutral H beam. Only the pure proton beam is selected, suitable for insertion into a circular 75 m radius accelerator called Booster, which delivers a total of 8 GeV proton beam to the Main Injector (MI) [28]. The MI is a 3,319.4 meter circumference synchrotron that accelerates the beam proton up to 150 GeV. Since the Main Injector circumference is seven times the Booster circumference, beam from multiple consecutive Booster cycles, called batches, can be injected around the Main Injector. The MI supports various operational modes for delivering beam across the complex, but we will focus on the one of interest in this work. The MI provides 120 GeV protons in a 4 sec long slow-spill extracted to the Switchyard as a primary beam source for the production of secondary and tertiary beams, either inside the Meson Test Beam Facility or at other fixed-target experiments (see figure 4.2) [29].

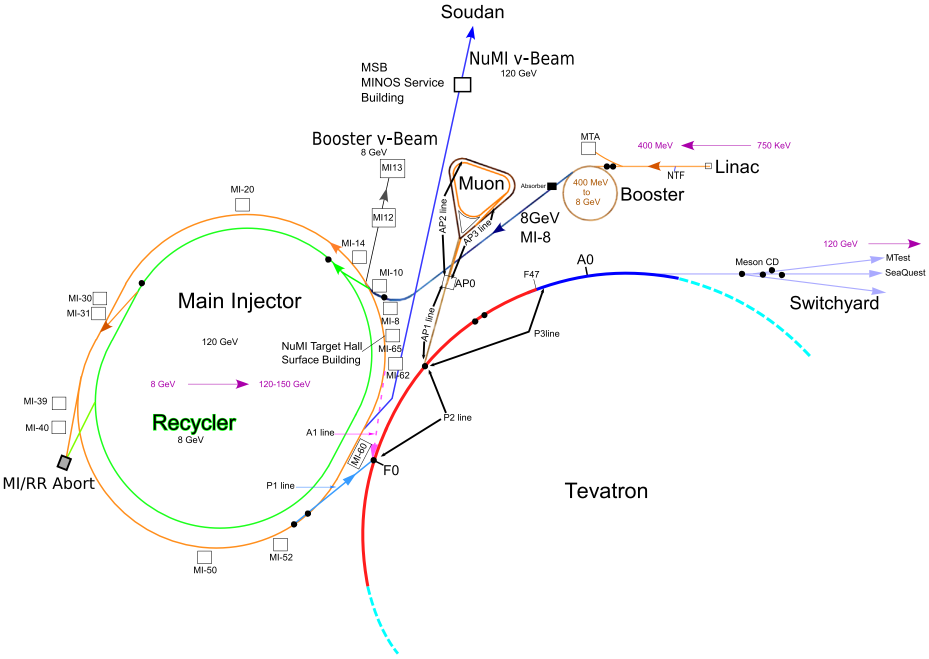

Figure 4.1 | Fermilab accelerator chain
The image is a map of the Fermilab accelerator chain, starting at the RFQ/LINAC, up to to the Main Injector. After 2011, only a section of the Tevatron was kept operational in order to deliver beam spills to the Switchyard, SeaQuest and MTest [30].

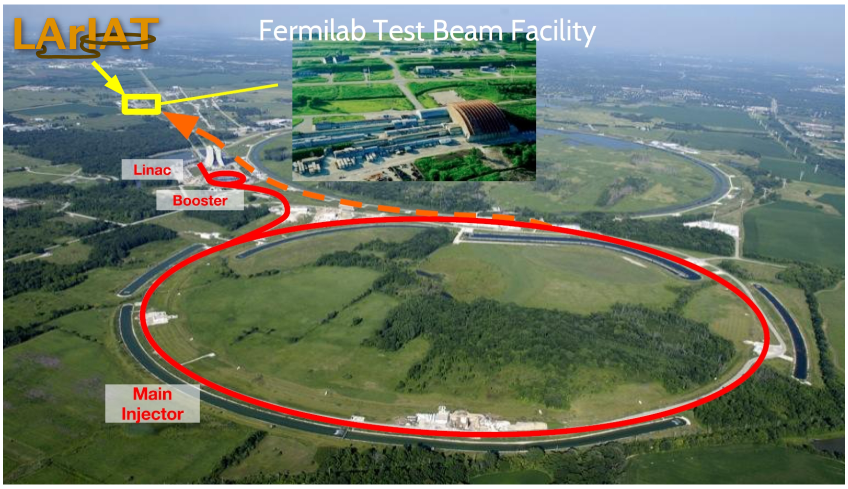

Figure 4.2 | LArIAT's primary beam
View of LArIAT's primary beam and LArIAT's location near to it [20].

4.1.2 Secondary Beam

After entering the MTest, the primary beam is directed to a copper target, whose interaction create a secondary particle beam of collimated pions of energies from 8 GeV to 64 GeV (see figure 4.3) [31].

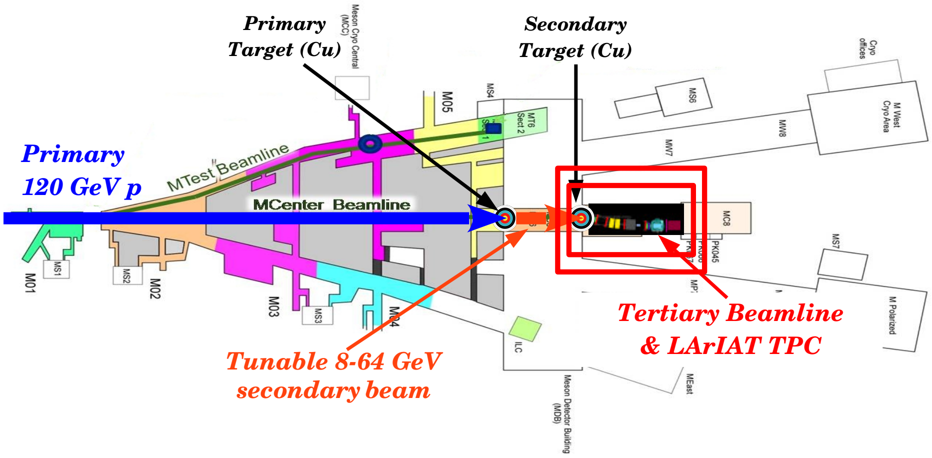

Figure 4.3 | LArIAT's secondary beam
Map of LArIAT's secondary beam, showing the short distance between the primary and the secondary copper targets [20].

4.1.3 Tertiary Beam

The particles from the secondary beam are used to produce the tertiary beam, which is an apparatus that consists of a copper target, a collimator system, and two bending magnets. The collision of the secondary beam with said target produces batches of mainly pions, protons, lower rate electrons, muons, and kaons, down to about 0.2 MeV/c, in a 13° angle (see figure 4.4). A pair of dipole magnets bend each spill in a 10° angle. Changes in the field intensity in the magnets provides the possibility to tune the particle momenta within a range that varies from 0.2 to 2.0 GeV/c.

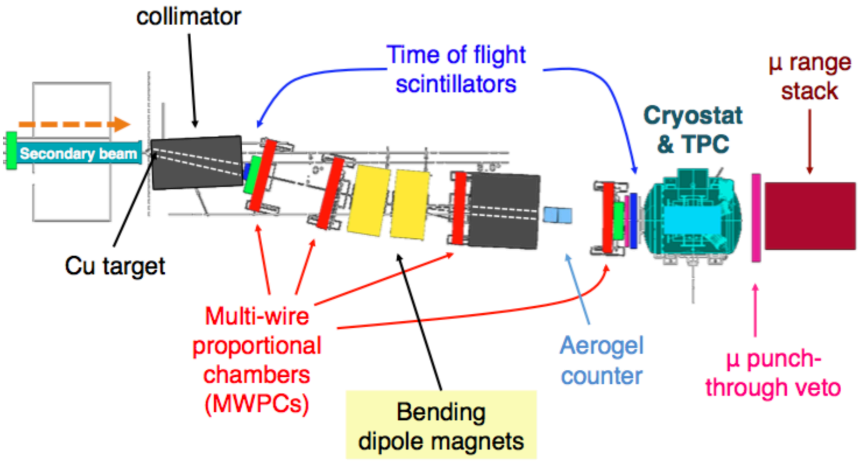

Figure 4.4 | LArIAT's tertiary beam
LArIAT's tertiary beam and full LArIAT's detector chain map [19].

4.2 Beamline Detectors

4.2.1 Magnets and Multi-Wire Proportional Chambers

Multi-wire Proportional Chambers (MWPC)

Multi-Wire Proportional Chambers were first constructed and operated by G. Charpak in 1967-68. They are detectors specially interesting to high energy physics due to their good time resolution, good position accuracy, and self-triggered operation.

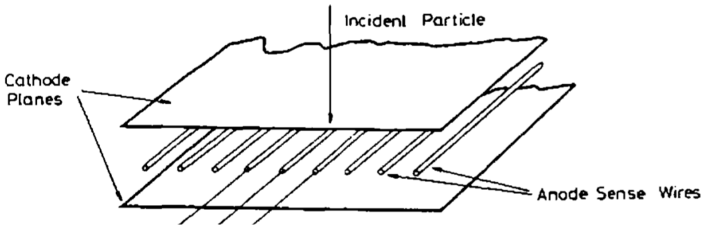

Figure 4.5 | Multi-wire Proportional Chambers Schematic
Figure shows a basic schematic of multi-wire proportional chambers [32].

Multi-wire Proportional Chambers (MWPC)

MWPC are constructed by a plane of wires at high voltage (anode) which run through a chamber with conductive walls held at ground potential (cathode). The chamber is then filled with a carefully chosen gas. The passage of a particle through the gas produces a set of ionization processes. The free electrons from the ionizations are accelerated by the electrical field towards the wire planes, ionizing more atoms in their path. The cascade reaction caused by the drift of the electrons is detected by the sense wires. The time and intensity of the pulses from all the wires provide a mean to reconstruct the trajectory of the original particle.

LArIAT's Magnets and Multi-Wire Proportional Chambers

LArIAT has two pairs of MWPC, one before, and one after a set of bending magnets (see figure 4.7). Each of the pairs is used to identify the direction of the through-going particle. The measurement of the angle α between each trajectory (i.e., before and after the particle being deflected by the magnet), provides the necessary information to determine its momentum (see figure 4.8).

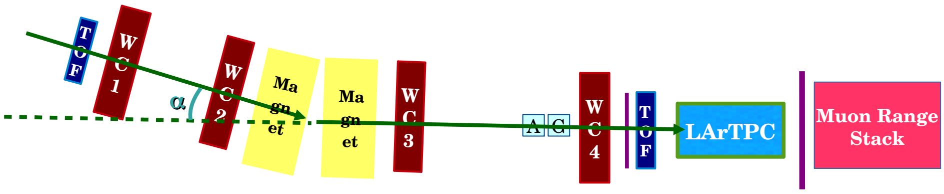

Figure 4.6 | The defined α angle in LArIAT's beamline
The α angle is the angle between the incident and deflected track by the bending magnets. The setup allows the measurement of the momentum of a through-going particle [20].

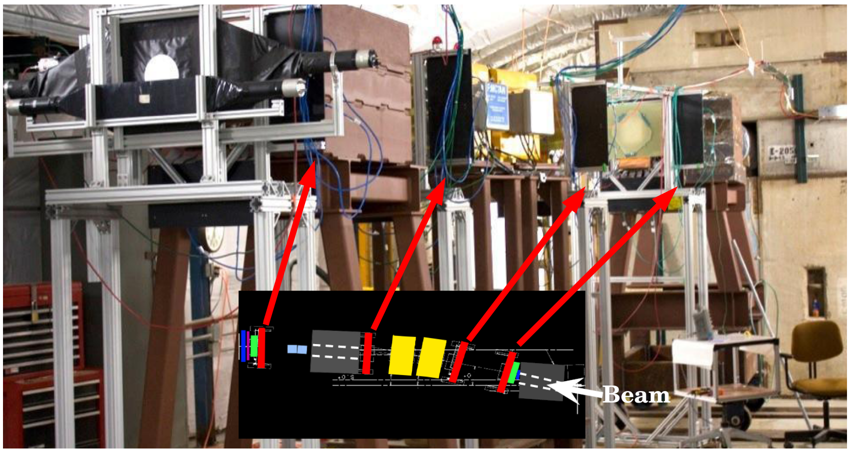

Figure 4.7 | MWPC's position in LArIAT
The image compares the schematic view of the LArIAT apparatus with the picture of the experiment. The red arrows are pointing to their corresponding real positions in the photo of the LArIAT apparatus [20].

4.2.2 Time Of Flight (TOF)

Scintillator Counters

Plastic scintillators are polymers that can be used for detecting charged particles within a wide energy range. The concept is based on the fact that the passage of a particle through such polymers results in an energy loss of the particle, which causes the polymer to go through an ionization process, either through bremsstrahlung effect or by inelastic collisions. The material then re-emits the absorbed energy in the form of light, in a process called scintillation [33]. In order to detect such light signal, photomultipliers (PMT) are used. They detect and amplify photon signals, producing an electric current as the output. PMTs are composed by an evacuated glass tube with a photocathode, several dynodes and one anode (see figure 4.9). The mechanism that produces a current induced by a photon interaction is the fact that the photon knocks out an electron from the photocathode, which is accelerated towards the dynodes. The amplification process is carried forward by the several dynodes. Each dynode is set to be at a higher voltage than the previous one and, as such, the electrons that are accelerated towards the next dynode cause more electrons to be knocked out, resulting an avalanche of electrons which,

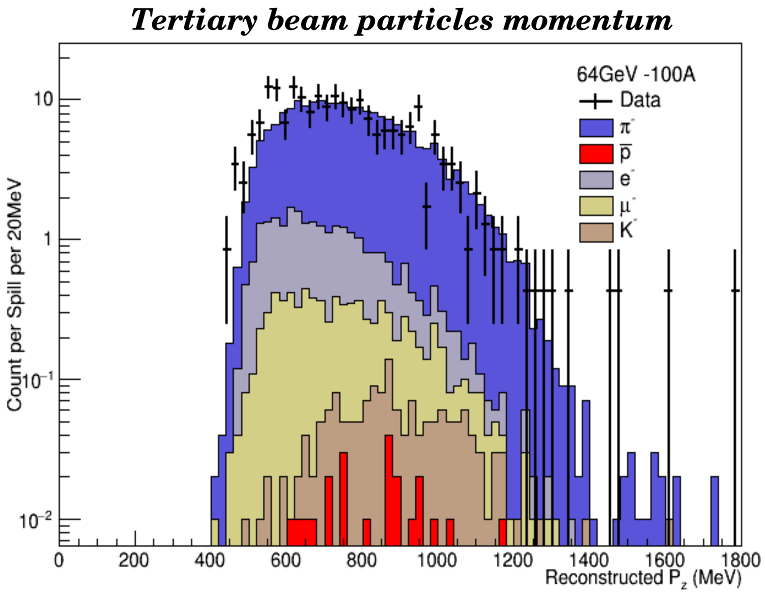

Figure 4.8 | LArIAT's tertiary beam particles momentum reconstruction
The plot shows the simulated and reconstructed particle momentum, which was reconstructed based on the angle α [20].

at the end, is measured as an electric current signal. Said electrical signal is proportional to the energy deposited in the polymer

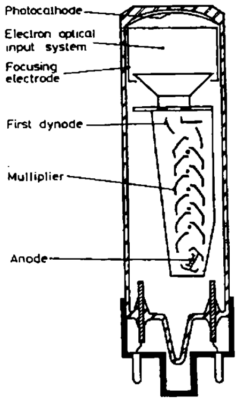

Figure 4.9 | Scheme of a photomultiplier
The figure shows the schematic of a photomultiplier tube, which encompasses a hollow glass tube, a photocathode, several dynodes and an anode [32].

A scintillator counter is composed by the scintillator polymer board and one or more photomultipliers (see figure 4.10).

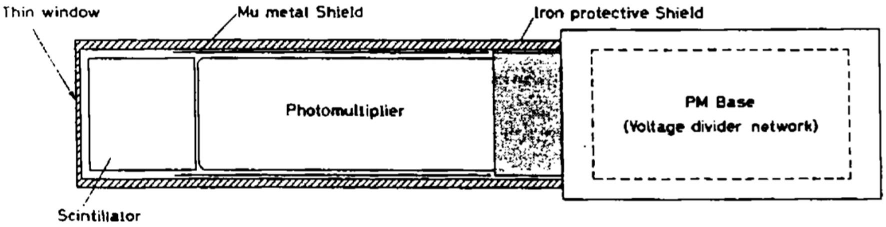

Figure 4.10 | Scintillator counter
Figure shows a basic scintillator counter, which is composed by attaching a PMT into a scintillator [32].

LArIAT's TOF

LArIAT has two scintillator detectors positioned at the start and at the end of the beamline (see figure 4.11). These two detectors allow the discrimination between particle species by measuring the time that the particle took to travel from the target to the TPC (hence, the name "Time of Flight"). This measurement allows the distinction between protons, kaons, and the combined category of muons, pions and electrons (see figure 4.12) [34].

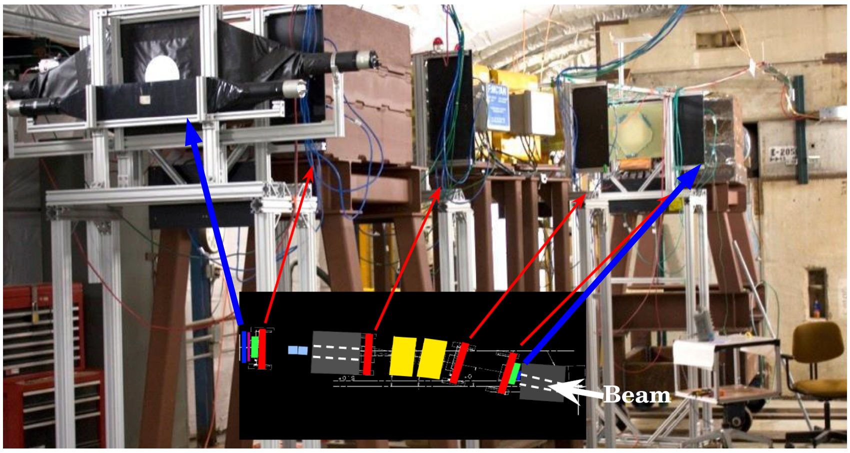

Figure 4.11 | LArIAT's TOF detectors position
The image shows the TOF position in both LArIAT schematic and photograph, being pointed to their corresponding real positions by the two blue arrows [20].

4.2.3 Aerogel Cherenkov Counters

Cherenkov Counters

Cherenkov radiation is an effect in which a particle emits photons when it passes through a dielectric medium faster than the speed of light in said medium. As such, the condition in

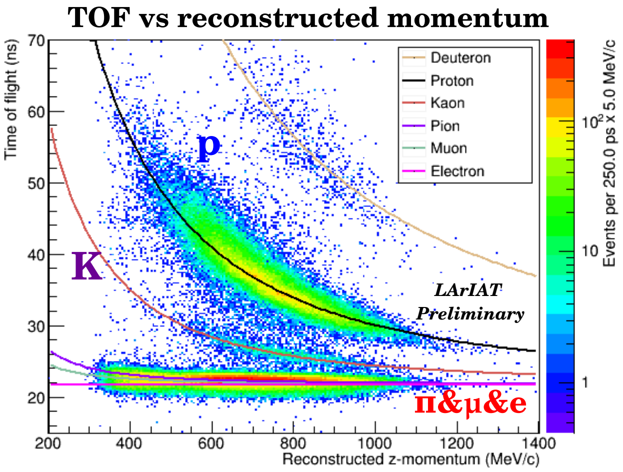

Figure 4.12 | TOF versus reconstructed momentum
The plot shows the Time of Flight as a function of reconstructed z-momentum. Different particles have different distributions, which allows for particle identification. It is important to notice that pions, muons, and electrons have very similar distributions, being impossible to distinguish them via this technique. [20].

which Cherenkov radiation is emitted is described as

$$v > \frac{c}{n}, \tag{4.1}$$

where v is the particle's velocity, c is the speed of light in vacuum, and n is refraction index of the medium. When such cases occur, an electromagnetic shock wave with a characteristic blue glow [32] is created by the through going particle.

Cherenkov detectors/counters use this property as their basic concept. As such, they are composed by a material with a chosen refraction index and a photomultiplier that is configured to measure the Cherenkov light produced by the passage of a relativistic particle.

LArIAT's Aerogel Cherenkov Counters

LArIAT has two Cherenkov counters made of a material called aerogel. It is a solid material of extremely low density, produced by removing the liquid component from a conventional gel (see figure 4.13). The two detectors are positioned behind the second collimator and provide an additional method of particle identification, which is specially able to separate muons and pions. One of the detectors has an aerogel with index of refraction of 1.11, while the other has an index of refraction of 1.057.

The concept is that in the 200-300 MeV/c momentum range, muons will produce Cherenkov radiation on the first detector, while pions will not produce it in either of the detectors. In the 300-400 MeV/c range, muons will produce Cherenkov radiation in both detectors and pions only in the first. In this scenario, grouping information from the aerogel and MWPC allows for a good method of identification between these two particles within the 200 to 400 MeV/c

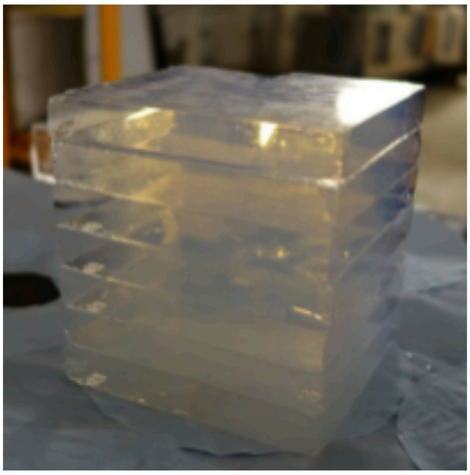

Figure 4.13 | LArIAT's aerogel
Picture of the aerogel material used on one of LArIAT's Cherenkov detectors [35].

momentum range (see table 4.1).

Momentum range	n = 1.11	n = 1.057
200 – 300 MeV/c	μ	none
300 – 400 MeV/c	μ and π	μ

Table 4.1 | LArIAT aerogel detectors
LArIAT has two Cherenkov detectors, one with refraction index of 1.11 and the other with refraction index of 1.057. In the 200-300 MeV/c range, muons will produce Cherenkov light only in the first detector, while pions will produce in neither. In the 300-400 MeV/c range, both muons and pions will produce Cherenkov light in the first detector, but only muons will produce Cherenkov light in the second. This scheme allows the separation between muons and pions in the 200-400 MeV/c momentum range. [35]

4.2.4 Muon Range Stack (MuRS)

Muons and pions have similar masses, as can be seen in table 4.2, which means that the beamline detectors are not always capable of differentiating them.

Particle	Mass (MeV/c^2)
Pion	139.57
Muon	105.66

Table 4.2 | Muon and pion mass

In the case of a fully contained event in the LArTPC, it is possible to use the PIDA method, described in section 3.2.6, to determine whether the particle is a muon or a pion. In the case where the particle is not fully contained and travels beyond the back of the cryostat, the PIDA peaks for both pions and muons overlap, making it impossible to distinguish between the two particles. In such cases, a new accessory detector is needed. One fundamental difference between muons and pions is the fact that muons are leptons and pions are mesons. As such, the latter can interact hadronically, while leptons cannot. This difference is the key concept used by the MuRS detector to differentiate them.

Detector description

The Muon Range Stack is located after the LArTPC, with the purpose to detect the non-fully-contained pions and muons that traverse the rear face of the cryostat. The detector is composed of 11 layers of iron slabs of different thicknesses, separated by a gap of $\sim$3 cm from each other, yielding a total length of 118 cm. The gaps are added to allow the installation of scintillator planes. In the current design of the detector, scintillator planes were installed in only 4 of these gaps.

The number of installed scintillator planes changed over time. During the first data taking run, the MuRS had 4 scintillator planes in total, with each of the scintillator planes being formed by 4 scintillator paddles connected in parallel (see figure 4.14).

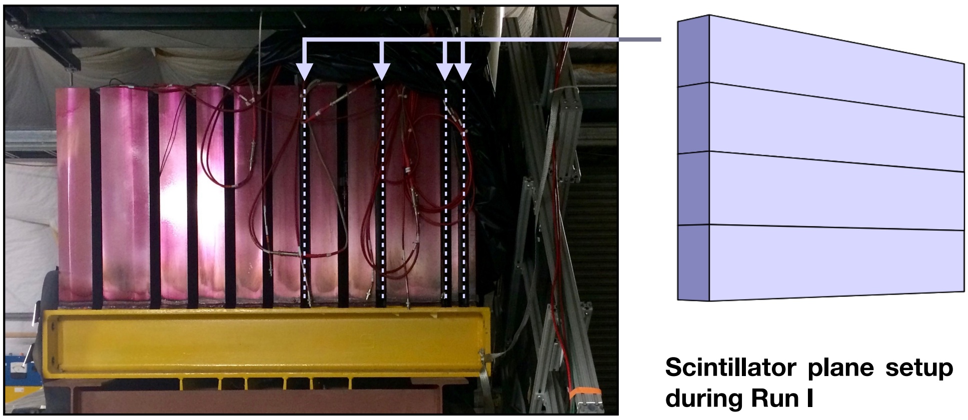

Figure 4.14 | Muon range stack detector in LArIAT's first run
Muon range stack detector in LArIAT's first run. There were four layers of scintillator planes. Each of the scintillator planes is composed of 4 scintillator paddles, horizontally positioned.

Between the first and second runs, 4 more scintillator planes, identical to the previous one, were added to the detector. Each new plane was installed in the same air gap that contained a previous scintillator plane, but rotated 90° with respect to the former plane. This created an arrangement of 4 pairs of scintillator planes, each pair encompassing 4 horizontal paddles and 4 vertical paddles (see figure 4.15). The reason for this setup was to allow for 3D track reconstruction, as each pair of planes could provide a 3 dimensional space coordinate.

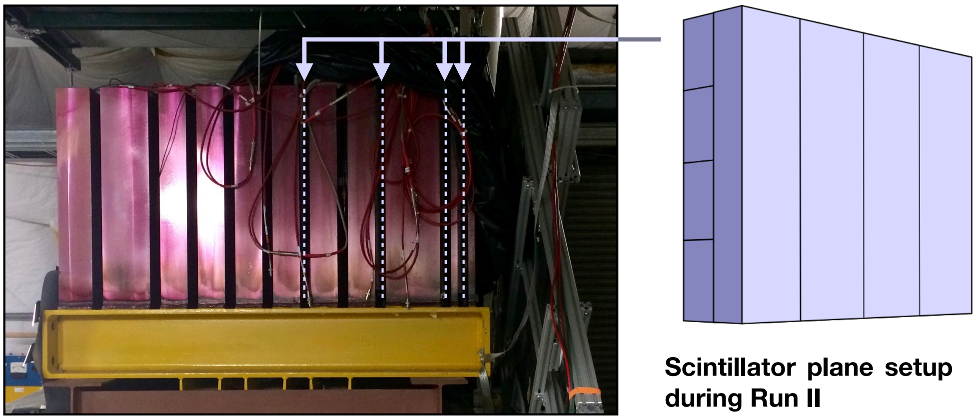

Figure 4.15 | Muon Range Stack detector during LArIAT's second run
Figure shows the setup of the Muon Range Stack detector during the second data taking run, presenting the eight layers of scintillator planes. Each of the scintillator planes is composed of 4 scintillator paddles. Four planes have horizontally positioned paddles and the other four have vertically positioned paddles. The scintillators are installed in pairs, with each plane being rotated 90° with respect to the other.

The detailed schematic of the detector can be seen on figure 4.16, which shows its final scintillator plane configuration, the thickness of each iron slab, and the distance between each slab. In total, MuRS has 88.6 cm of metal along the beam direction.

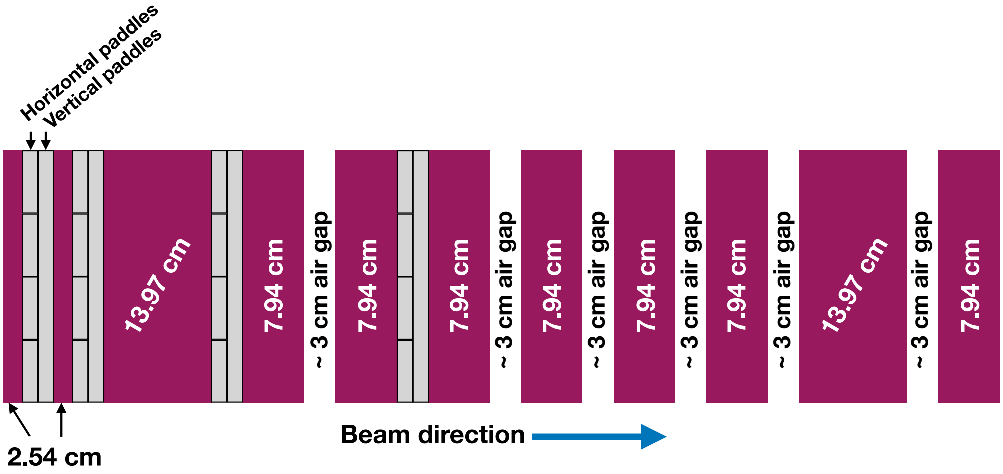

Figure 4.16 | Schematic of the Muon Range Stack detector
Figure shows the iron layers of the Muon Range Stack detector along with their thicknesses, the air gaps, and the locations of the scintillator paddles.

Muon and pion separation challenges

Given the energy range of the tertiary beam, and considering the energy loss of particles through the various LArIAT detectors, it is reasonable to consider the momentum of most pions and muons that reach the MuRS to be ranging from $0.1 < p < 1$ GeV/c. Figure 4.17 shows that the mean differential energy loss in iron for muons and pions are, respectively, 1.95 MeV/g.cm^2, and 2.25 MeV/g.cm^2. Thus, to estimate the average energy loss for those particles for each MuRS plane, one could use

$$E_{\text{loss}} = \frac{dE}{dx}\rho_{\text{iron}}d, \tag{4.2}$$

where dE/dx is the mean energy loss rate, ρ_{iron} = 7.87 g/cm^3 is the iron density, and d is the thickness of the slab. Considering the thickness of each slab, the average energy losses per particle while traversing each MuRS' iron slab is presented in table 4.3, which shows that only pions or muons with a momentum larger than 1568.88 MeV/c, and 1359.70 MeV/c, respectively, should reach the rear end of the Muon Range Stack.

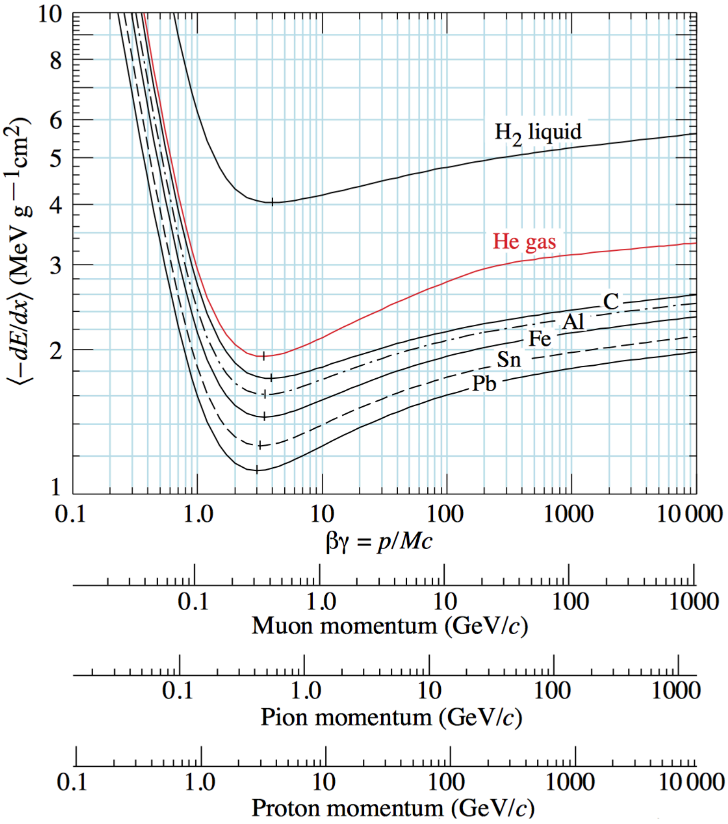

Figure 4.17 | Mean energy loss rate for different materials and particles.
Mean energy loss rate in liquid (bubble chamber) hydrogen, gaseous helium, carbon, aluminum, iron, tin, and lead.

Layer	Slab thickness (cm)	E_{loss} (MeV) [0.1 GeV < E < 1 GeV]	
		Pions	Muons
1	2.54	44.98	38.98
2	2.54	44.98	38.98
3	13.97	247.37	214.39
4	7.94	140.60	121.85
5	7.94	140.60	121.85
6	7.94	140.60	121.85
7	7.94	140.60	121.85
8	7.94	140.60	121.85
9	7.94	140.60	121.85
10	13.97	247.37	214.39
11	7.94	140.60	121.85
Cumulative	**88.60**	**1568.88**	**1359.70**

Table 4.3 | Pion and muon energy loss per iron slab
Table shows the energy loss in each each metal slab of the MuRS for pions and muons considering the energy of both pions and muons ranging between 0.1 GeV and 1.0 GeV. The table is calculated by considering the average differential energy loss of each particle within said energy range, whose values are dE/dX = 2.25 MeV.cm^{-2}.g^{-1} for pions and dE/dX = 1.95 MeV.cm^{-2}.g^{-1} for muons. The iron density considered is 7.87 g/cm^3.

4.3 The Main Detector

4.3.1 The Cryostat

LArIAT's cryostat is cylindrical, stainless-steel, vacuum-jacketed, super-insulated, and was originally ArgoNeuT's. As such, it had to suffer a series of adaptations in order to make it adequate for being used in a charged particle testbeam [18]. The inner vessel supports 550 L of LAr (76.2 cm of diameter and 130 cm of length) and can be seen in figure 4.18.

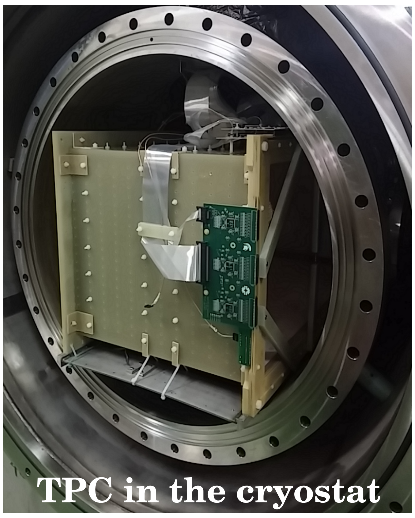

Figure 4.18 | LArIAT's TPC Inside Cryostat
Figure shows the borders of the cryostat enclosing the TPC used by LArIAT [20].

4.3.2 The LArTPC

The ArgoNeuT TPC was also refurbished for LArIAT. It is a 170 liters (47 w × 40 h × 90 l cm^3) of active volume TPC, under a 500 V/cm drift field, with a maximum drift length of 47 cm (see figure 4.19). The refurbishment was necessary to accommodate cold electronics and add three new wire planes, although their geometry was kept the same as in the old ArgoNeuT.

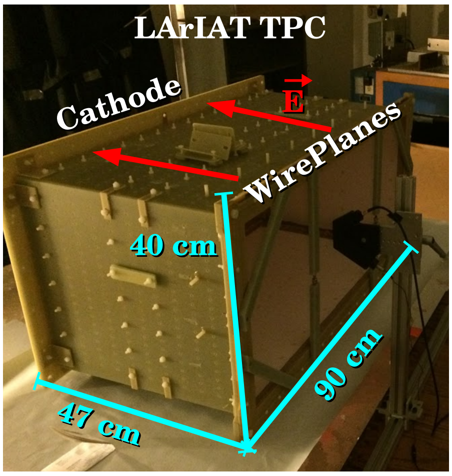

Figure 4.19 | LArIAT TPC
Picture shows the TPC used by LArIAT, along with its dimensions, the cathode, the wire planes, as well as the the direction of the electric field [20].

The first wire plane is non-instrumented and shapes the electrical field near the wires, and shields them from induction due to drifting charge. It contains 225 wires vertically oriented with respect to the ground and perpendicular to the beam axis. The other two are the wire planes that are used to detect the ionization charge. The first is the induction wire plane and the second the collection plane. In both of them, the wires are 4 mm spaced and angled at $+/-$ 60° relative to the beam direction.

4.3.3 The Light Collection System

LArIAT's light collection system has two cryogenic high-quantum-efficiency photomultipliers and three silicon photomultipliers[1] (SiPMs) (see figure 4.20). A reflective dielectric substrate foil is deposited in a layer of tetraphenyl butadiene (TPB). This reflector foil covers the walls of the field cage. The ultraviolet photons from LAr scintillation are absorbed and reemitted in the form of visible light by the TPB (see figure 4.21). This new technique allows light detection with minimal losses.

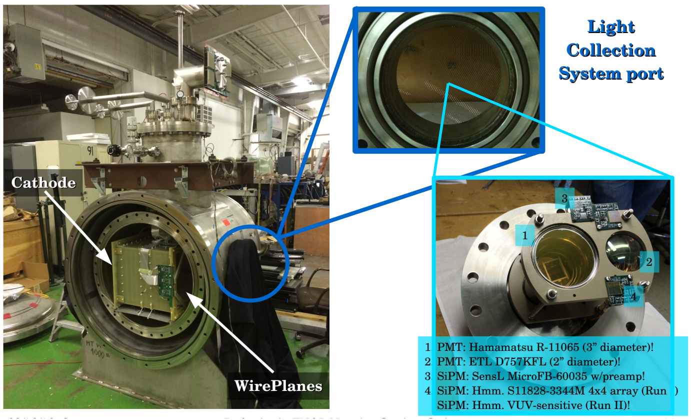

Figure 4.20 | LArIAT's light collection system
Picture shows the position of the light collection system port in the cryostat and the position of the PMTs and SIPMs [20].

---

[1] Silicon photomultipliers are detectors capable of sensing, timing and quantifying low-light signals down to the single-photon level. As a solid-state sensor, it features low-voltage operation, insensitivity to magnetic fields, mechanical robustness and uniform response. It consists of a matrix of pixels connected in parallel. Each pixel is a photodiode and a quench resistor in series. The photodiode is operated a few volts above its breakdown voltage such that electrical breakdown occurs if a photoelectron is generated within the active volume [36].

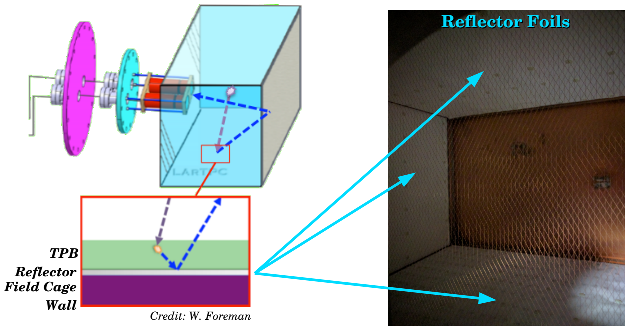

Credit: W. Foreman

Figure 4.21 | TPB reflector foils
The figure shows a schematic of the reflector foils and its work inside the TPC, a schematic of the absorption and reemission inside by the TPB and a picture of the reflector foil coverage in LArIATs TPC [20].

Chapter 5

MuRS Simulation Using Geant4

5.1 Overview of Monte Carlo Simulation

A Monte Carlo (MC) simulation of the detector response to the passage of particles through it is a necessary tool to assess the efficiency of the reconstruction method and a way to inform (at least part of) the necessary cuts of any analysis. The interaction between particles and the detector is carried forward by Geant4 [38–40], which is a simulation software tool widely used in High Energy Physics for studying the passage of particles through matter. LArIAT's full beam line simulation is still under development, so it is impossible to include it in the current simulation chain. Given this limitation, the single particle gun was used in this study. This tool simulates particles on a one-by-one basis, with predefined starting position and momentum, in order to make it traverse through any currently-implemented part of the experiment. Although the single particle gun is a powerful tool, some inaccuracies need to be acknowledged, such as [37]:

- It only fires one type of particle with a predefined energy distribution at a time, not mimicking the full tertiary beam composition
- It does not take into account the interaction of particles with the detectors prior to the MuRS. With the lack of any expected distribution of energy, position, momenta, and composition of the beam prior to the MuRS, the resulting simulated output is inaccurate.

5.2 The simulated MuRS geometry

The current Geant4 geometry file used by LArIAT tries to include in its simulation the main components of the real beam line, as it is shown in figure 5.1 (a). Although partially constructed, some main components of the simulation are still not well defined, such as the magnetic field between the wire chambers. Figure 5.1 (b) provides a more detailed view of the Muon Range Stack Detector geometry, which shows the Punch Through, composed by two diagonal planes forming 45° with respect to the x-axis, and the Muon Range Stack itself. As mentioned before, the MuRS is a set of intercalated slabs of metal and scintillator planes. Four scintillator paddles comprise each scintillator plane. By the time of LArIAT's run I, the Muon Range Stack had only four scintillator planes, resulting in a total of 16 channels, all placed in a horizontal manner. Despite its low granularity and lack of 3D reconstruction capacity, its intercalated geometry, allied with the Punch Through, is enough for quantifying the penetration depth of a traversing particle.

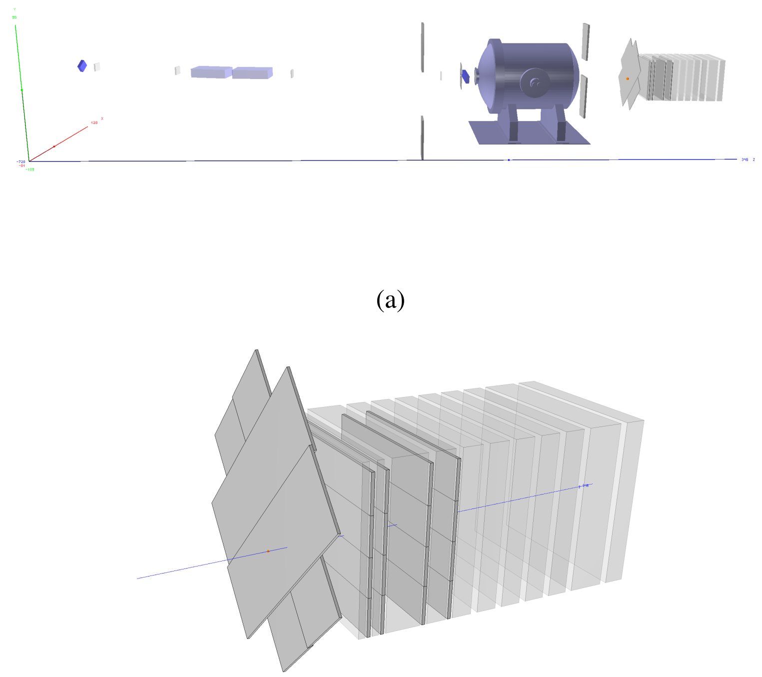

(a)

(b)

Figure 5.1 | LArIAT simulated geometry
(a) LArIAT's beam line geometry as in the Geant4 geometry file. The lower left corner corresponds to coordinates x = –81 cm, y = 0.109 cm and z = –720 cm. (b) LArIAT's Muon Range Stack Detector geometry as in the Geant4 geometry file, showing both the punch through detector, and the Muon Range Stack itself, which is composed by intercalated metal slabs and scintillator paddles.

5.3 Simulation description and input parameters

The data that was simulated for this analysis uses the single particle gun, which fires particles into the Geant4 geometry. It uses a set of chosen input variables, such as the particle's ID, energy range, (x, y, z) starting position, and (p_x, p_y, p_z) momenta. According to the geometry file, the ideal starting position for the simulated particles is at (25, 10, 200) cm, which corresponds to the center of the Punch Through in the xy-plane and to the z-position immediately prior to it.

In order to achieve the goals of this study, 2 large samples of pions and muons were simulated, producing a total of 100,000 particles each. The chosen energy range was kept identical in each sample, following a flat distribution that varied from 0 GeV to 1.8 GeV. Similarly, the starting position of the particles was uniformly distributed over the (x, y) plane, following a 20 cm wide flat distribution in each direction. The z coordinate, however, was fixed at 200 cm, as smearing the longitudinal starting position would produce a similar effect as varying the particles' valid energy range. The input parameters for both samples are summarized in table 5.1.

Simulation input parameters

	Pions	**Muons**
Sample size	100,000	100,000
Particle ID	±211	±13
Start[X, Y, Z] (cm)	[20, 5, 200]	–
σ[X, Y, Z]	[10, 10, 0]	–
P (GeV/c)	0.9	–
σ_P	0.9	–

Table 5.1 | Simulation input parameters
The table shows size and the chosen parameters for producing both pion and muon MC samples. The parameters are chosen in order to produce particles starting at the geometrical center of the Punch Through in the xy-plane, and immediately prior to it, with a kinetic energy ranging from 0 GeV to 1.8 GeV. Columns with "–" mean that the same values were applied in both samples.

5.4 Analysis

The output files of the simulation have an identical structure to the files produced by the data acquisition system of the experiment, except for the addition of the true information of the simulated particles. Such files are processed to produce a new set of n-tuple files that are well structured and include useful physical quantities, such as true particle ID, starting and ending vertices, trajectory directional cosines, starting energy, and so on, needed to analyze the simulated data.

5.4.1 Consistency checks

The first step prior to the analysis itself consists of producing a set of data plots for verification purposes. This is necessary to confirm that the output of the simulation is in agreement with the expected information from the input parameters. Figures 5.2, 5.3, 5.4, and 5.5, show the starting energy distribution of each sample, the (x, y) position of particles at the beginning and end of their trajectories, and the ID of the primary particles. The distributions confirm that the simulation ran correctly, and the production of the files necessary for the analysis is also working accordingly.

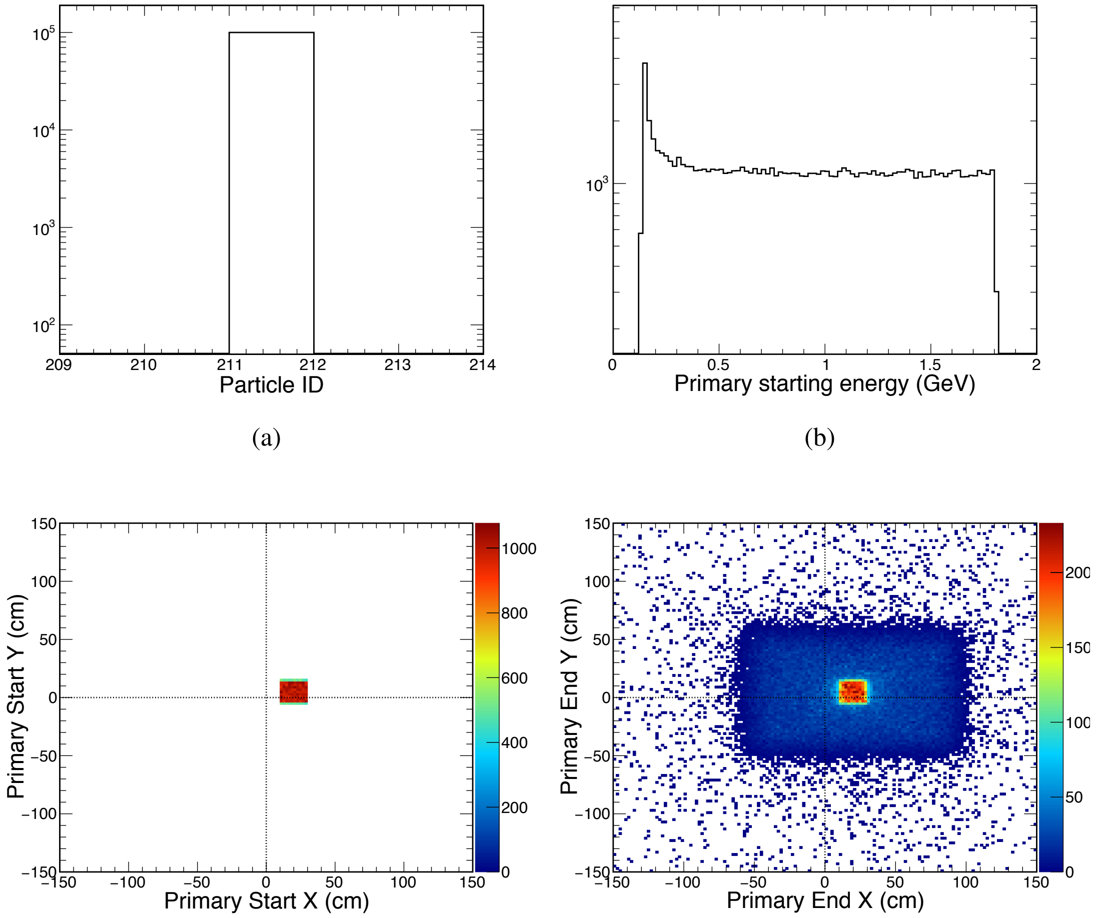

(a) (b)

(c) (d)

Figure 5.2 | Consistency plots for the π^+ sample
Figure shows (a) the number and ID, (b) the starting energy, (c) the starting position in the xy-plane, and (d) the ending position in the xy-plane, for the sample with π^+ as primaries.

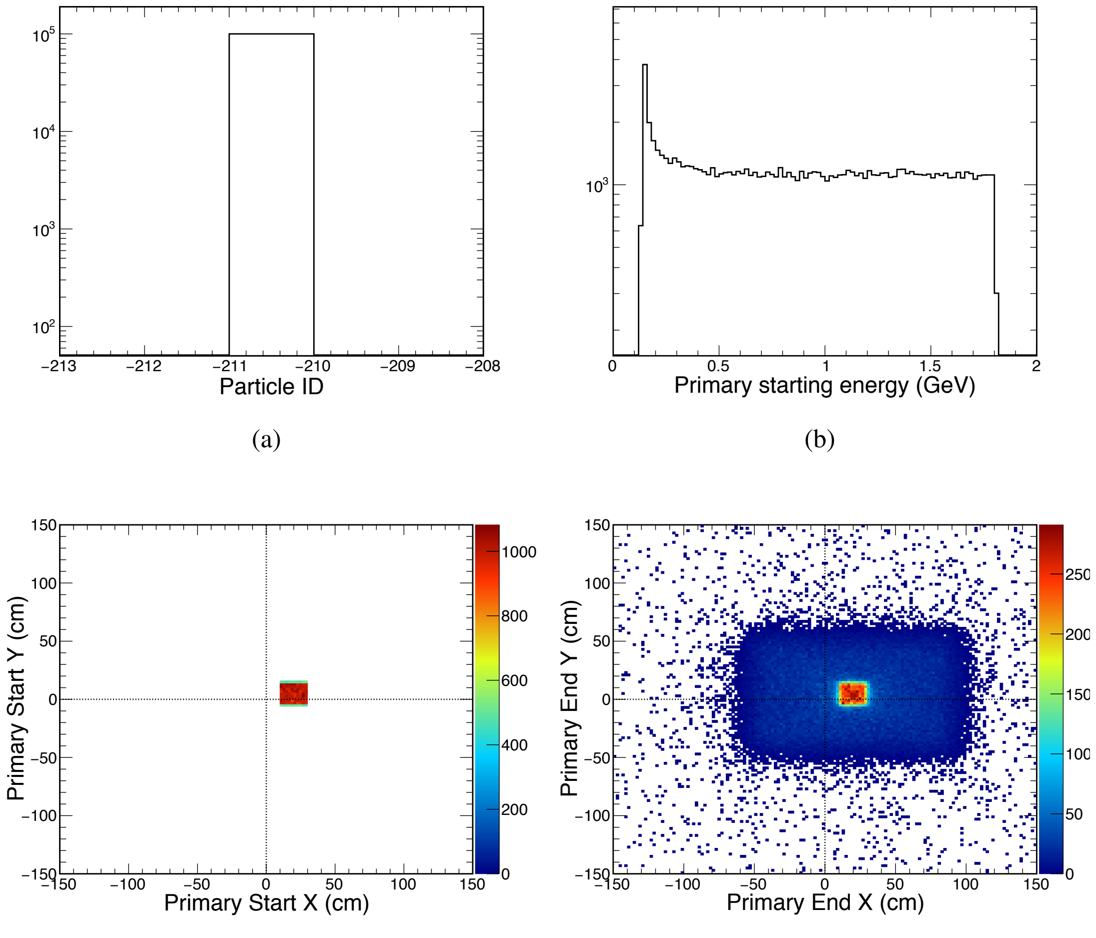

(a) (b)

(c) (d)

Figure 5.3 | Consistency plots for the π^- sample

Figure shows (a) the number and ID, (b) the starting energy, (c) the starting position in the xy-plane, and (d) the ending position in the xy-plane, for the sample with π^- as primaries.

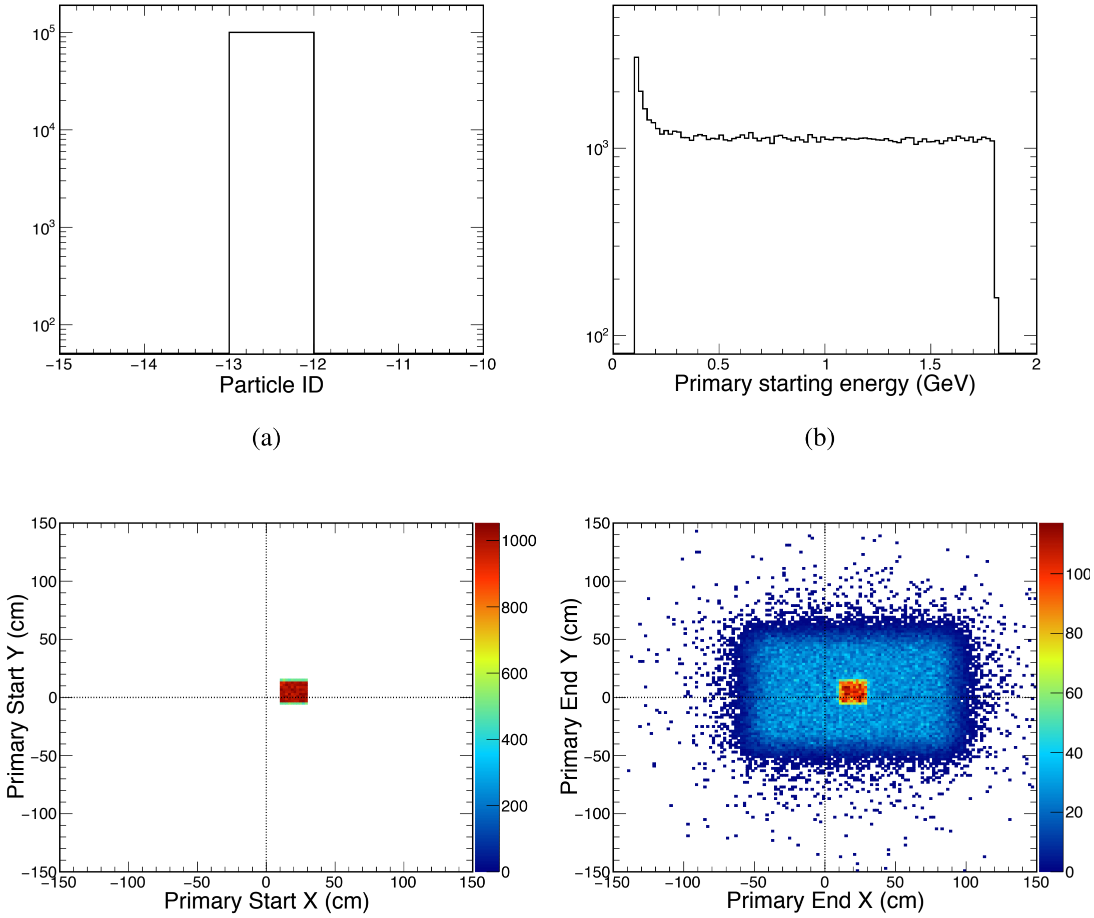

(a) (b)

(c) (d)

Figure 5.4 | Consistency plots for the μ^+ sample
Figure shows (a) the number and ID, (b) the starting energy, (c) the starting position in the xy-plane, and (d) the ending position in the xy-plane, for the sample with μ^+ as primaries.

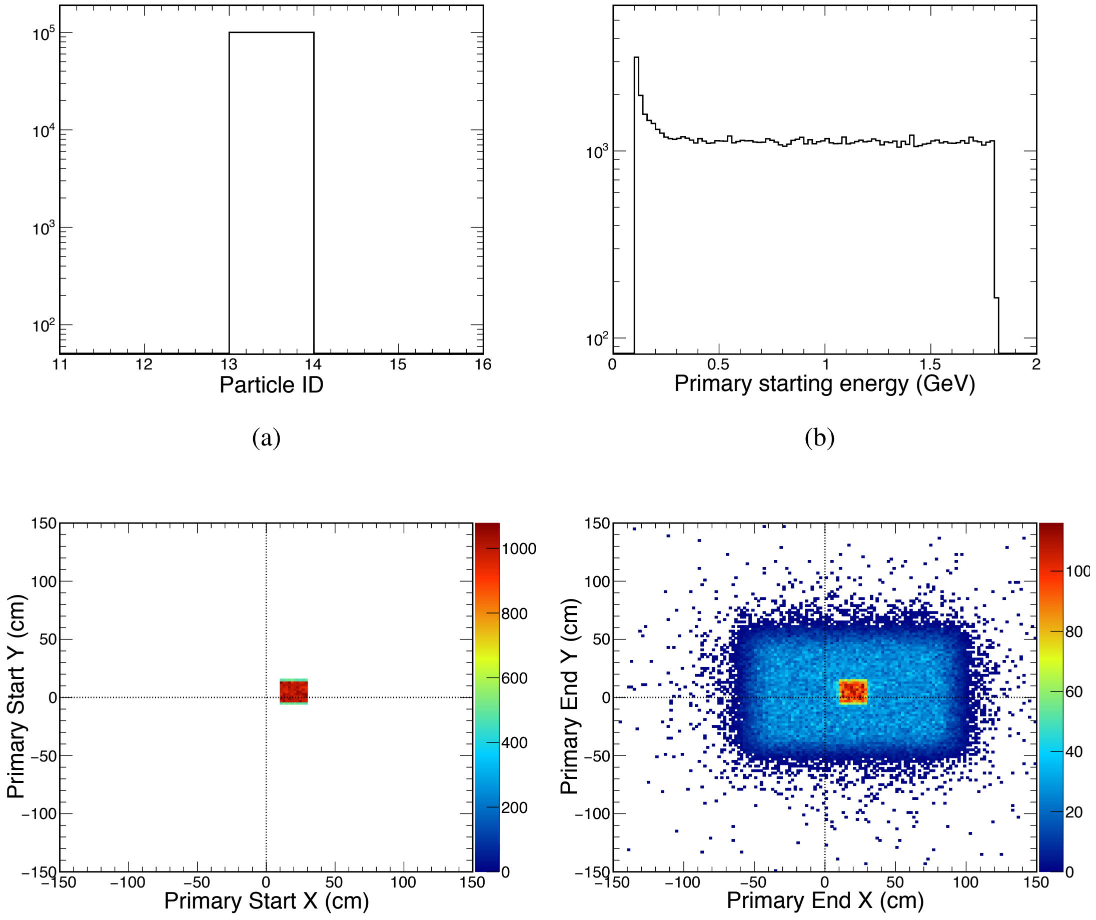

(a) (b)

(c) (d)

Figure 5.5 | Consistency plots for the μ^- sample
Figure shows (a) the number and ID, (b) the starting energy, (c) the starting position in the xy-plane, and (d) the ending position in the xy-plane, for the sample with μ^- as primaries.

5.4.2 Selection criteria

During the steering of the simulation, more muons and pions may be produced due to either decay (such as pions decaying into muons) or hadronic interactions of pions with the detector. As such, it is important to select only the primary particles of the simulation in order to avoid tagging penetration depths caused by secondary or further particles. To do so, two selection criteria are used to avoid including daughter particles into the final results:

- The starting vertex of the particle must be located at z = 200 cm.
- The selected particle must be a pion or a muon.

5.4.3 Definition of the penetration depths

The differentiation between pions and muons can be done by comparing the stopping z position of each primary particle and the different penetration depths of the MuRS detector. In this context, we define a particle's penetration depth as the positions of the void regions between every pair of metal slab of the MuRS. The first penetration depth represents the region where the first scintillator plane, closer to the Punch Through, is placed. Table 5.2 shows each penetration depth level, along with its z position, and if there is a scintillator paddle in it. The penetration depth of a said particle is defined as being the last predefined level prior to the real stopping z vertex of the particle (i.e., if a hypothetical pion stops at z = 268 cm, its penetration depth is labeled as 4). A visual representation of each penetration depth level is presented in figure 5.6.

Penetration depth level	z coordinate (cm)	Includes a scintillator plane
0 (Punch Through)	210	–
1	231	Yes
2	237	Yes
3	254	Yes
4	265	No
5	275	Yes
6	286	No
7	297	No
8	307	No
9	318	No
10	335	No

Table 5.2 | Definition of the penetration depths
The table shows the list of penetration depths, whose positions represent the center of the void regions between the MuRS iron slabs, along with the information of whether a said penetration depth has or not a scintillator plane in it.

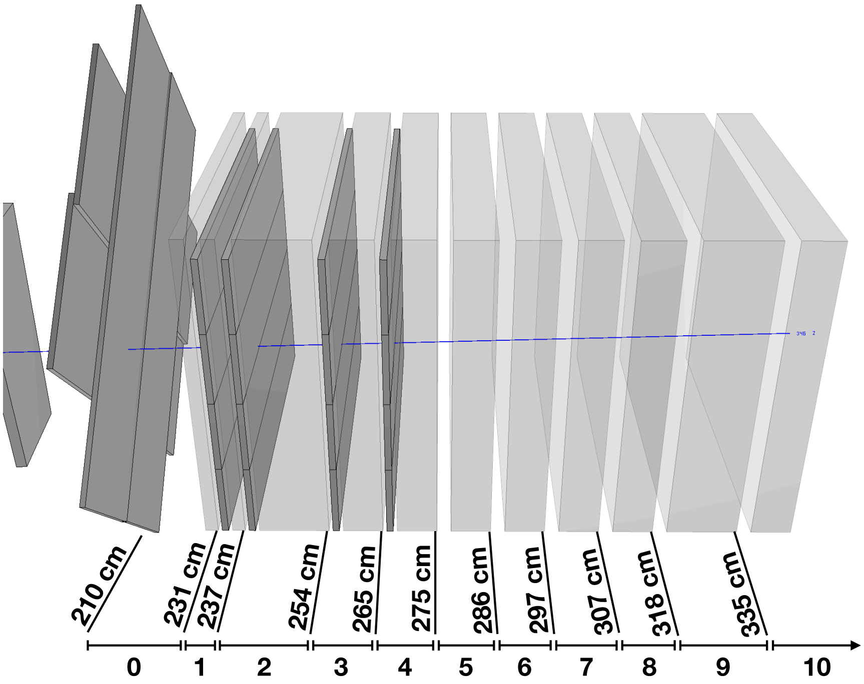

Figure 5.6 | Definition of the penetration depths
The figure shows the simulated MuRS along with the position and labeling of each defined penetration depth.

5.4.4 Analysis plan

The goal of the Muon Range Stack is to differentiate pions and muons by identifying stopping particles as pions, while considering the through-going ones as muons. The very low granularity of the detector provides a very rudimentary 3D track reconstruction. In this scenario, analyzing solely the penetration depth in the z coordinate of a traversing or stopping particle is a good first approximation for assessing the detector performance. As the goal can be simplified to the understanding of the penetration depth of the particle into the Muon Range Stack, the main important variables in this study are the particle ending position in the z coordinate and its starting energy. By counting the number of stopping particles at each defined penetration depth, it is possible to assess the capacity of the Muon Range Stack to identify pions from muons after each of its iron slabs. Such analysis not only provides a means to understand the current efficiency and purity of a selection criterion, given the current positions of the scintillator planes, but it provides a full picture of the detector's capacity, including the possibility of moving the scintillator planes to more efficient locations in a possible future data run.

The efficiency (e) and purity (P) are assessed at each depth of the detector, and are defined as being

$$e = \frac{\text{Number of } \pi \text{ at depth } i}{\text{Total number of } \pi} \tag{5.1}$$

$$P = \frac{\text{Number of } \pi \text{ at depth } i}{\text{Total number of } \pi \text{ and } \mu \text{ at depth } i}. \tag{5.2}$$

As such, these two definitions quantify the quality of a reconstruction based on its ability to identify a pion from a muon given its stopping position: The efficiency quantifies how many pions were identified as pions, considering all pions that traversed the detector, while the purity assesses the fraction of pions that are correctly tagged as pions. Although the number of counted particles comes from true information and, as such, carries no errors, the efficiency and purity can have their uncertainties calculated by considering the intrinsic statistical uncertainty of given a particle count. As all events are uncorrelated, the statistical uncertainty that arises from a given count of N particles is simply $\sqrt{N}$. Since both numerator and denominator in e and P represent particle counting, their associated error is

$$\frac{a \pm \delta a}{b \pm \delta b} = \frac{a}{b} \pm \frac{a}{b}\sqrt{\left(\frac{\delta a}{a}\right)^2 + \left(\frac{\delta b}{b}\right)^2}. \tag{5.3}$$

Finally, an energy cut was applied to the primary particles to be compatible and comparable to the calculation presented in table 4.3. Therefore, the energy cuts are

- 0.239 GeV $< E_\pi <$ 1.239 GeV
- 0.205 GeV $< E_\mu <$ 1.205 GeV

5.4.5 Results of the analysis

Figure 5.7 summarizes the correlation between the two main variables in the analysis, namely the end z position and starting energy of the primary particles. Many more pions stop within the different layers of the MuRS than muons, the vast majority of which ends up traversing the full volume of the MuRS detector. Table 5.3 provides the number of counted particles at each penetration depth. From the numbers presented in table 5.3 it is possible to assess the total number of particles at each depth and calculate the efficiencies and purities as a function of depth cut. Such number are presented in tables 5.4, and 5.5, which separates the numbers for positive and negative particles.

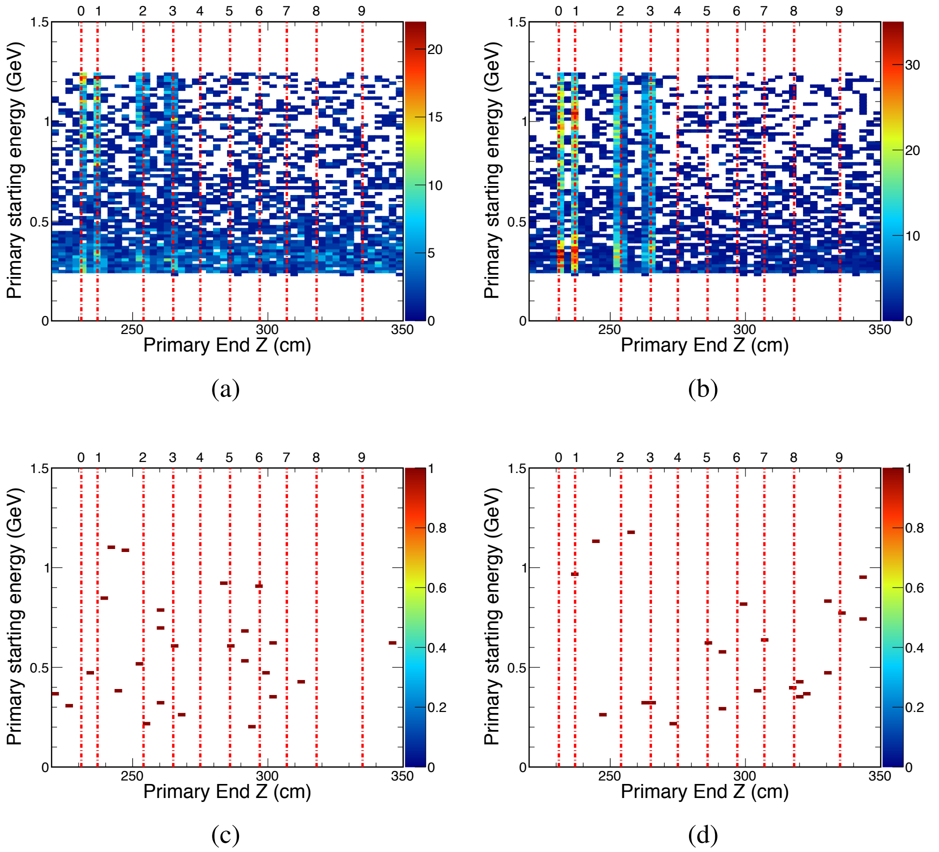

(a)

(b)

(c)

(d)

Figure 5.7 | Pion and muon ending z positions according to their starting energy
The figure shows the starting energy as a function of their stopping z position for (a) π^+, (b) π^-, (c) μ^+, (d) μ^-. The red vertical dashed lines show the position of each penetration depth.

Depth	**Number of particles**			
	π^+	μ^+	π^-	μ^-
0	2291	6	2973	2
1	677	1	1662	0
2	795	5	1509	3
3	634	4	1282	3
4	286	2	298	1
5	279	1	183	0
6	283	5	177	3
7	272	3	168	2
8	267	1	212	2
9	433	0	316	5
10	51397	57086	48669	56764
Total	**57614**	**57114**	**57449**	**56785**

Table 5.3 | Number of particles as a function of depth
The table presents the number of counted pions and muons at each predefined depth layer. The vast majority of both pions and muons reach the back end of the Muon Range Stack.

Cut at depth	**Number of particles**			**Efficiency and purity**	
	π^+	μ^+	Total	e	P
1	2968	7	2975	0.052 ± 0.001	$0.99^{+0.01}_{-0.02}$
2	3763	12	3775	0.065 ± 0.001	$0.99^{+0.01}_{-0.02}$
3	4397	16	4413	0.076 ± 0.001	$0.99^{+0.01}_{-0.02}$
4	4683	18	4701	0.081 ± 0.001	$0.99^{+0.01}_{-0.02}$
5	4962	19	4981	0.086 ± 0.001	$0.99^{+0.01}_{-0.02}$
6	5245	24	5269	0.091 ± 0.001	$0.99^{+0.01}_{-0.02}$
7	5517	27	5544	0.096 ± 0.001	$0.99^{+0.01}_{-0.02}$
8	5784	28	5812	0.100 ± 0.001	$0.99^{+0.01}_{-0.02}$

Table 5.4 | Efficiencies and purities for π^+ and μ^+ as a function of depth cut
The table shows the number of positive pions and muons counted after going through i detector depths, along with the expected efficiency and purity of the pion/muon identification method. As expected, confidence of the identification improves as more metal slabs are included.

Cut at depth	Number of particles			Efficiency and purity	
	π^-	μ^-	Total	e	P
1	4635	2	4637	0.081 ± 0.001	$0.99^{+0.01}_{-0.02}$
2	6144	5	6149	0.107 ± 0.001	$0.99^{+0.01}_{-0.02}$
3	7426	8	7434	0.130 ± 0.001	$0.99^{+0.01}_{-0.02}$
4	7724	9	7733	0.134 ± 0.002	$0.99^{+0.01}_{-0.02}$
5	7907	9	7916	0.138 ± 0.002	$0.99^{+0.01}_{-0.02}$
6	8084	12	8096	0.141 ± 0.002	$0.99^{+0.01}_{-0.02}$
7	8252	14	8266	0.144 ± 0.002	$0.99^{+0.01}_{-0.02}$
8	8464	16	8480	0.148 ± 0.002	$0.99^{+0.01}_{-0.02}$

Table 5.5 | Efficiencies and purities for π^- and μ^- as a function of depth cut
The table shows the number of negative pions and muons counted after going through i detector depths, along with the expected efficiency and purity of the pion/muon identification method. As expected, confidence of the identification improves as more metal slabs are included.

5.4.6 Discussion of the results

The simulation indicates that, for the structure of the MuRS paddles built, the efficiency and purity are, respectively, in the best case scenario at 8.1$\%$ and 99$\%$ for π^+, while being at 13.4$\%$ and 99$\%$ for π^-. By considering that the estimated through-going muon contamination on the pion cross-section analysis published by LArIAT in 2016 is 3$\%$ (see Appendix C.1), the improvement on the uncertainty would barely be tangible.

The detector efficiency and purity can be slightly improved by instrumenting the whole steel structure with paddles. This will push the numbers up to e = 10.0$\%$ and p = 99$\%$ for π^+, and e = 14.8$\%$ and p = 99$\%$ for π^-.

The theoretical predictions presented on section 4.2.4 estimates that only pions or muons with a momentum larger than 1568.88 MeV/c, and 1359.70 MeV/c, respectively, would be able to completely cross the MuRS steel structure, but the simulation shows that even particles with a momentum below 1 GeV are capable of traversing its full length.

This inconsistency between the theoretical prediction and the simulation can have a number of sources, with the most likely being

- The theoretical predictions made on this work are too simplistic and do not consider in detail the interaction energy loss for each of the momenta of the momentum range.
- The Geant4 software includes more possible interaction scenarios than the ones considered in the 4.17 results.
- There is an error in the geometry file used by the LArIAT collaboration.

Chapter 6

Conclusion

The theory behind the operation and design of Liquid Argon Time Projection Chambers was described, along with the prospect future experiments based on this technology. The main goals, as well as the experimental apparatus of the LArIAT experiment were presented, with a higher focus on the Muon Range Stack Detector, which was the main topic of this study. This analysis proposal was a Monte Carlo simulation of the Muon Range Detector, aimed to assess the capacity of the detector to correctly identify pions and muons. The necessity of this work rests on the goal to produce a more precise pion-argon cross-section measurement, whose uncertainty caused by non-well-identified pions and muons is at the order of 3% C.1. A set of 4 large samples, with 400,000 particles, was simulated to assess the efficiency and purity of the detector considering a particle identification method based solely on the depth reached by a stopping pion or muon into the MuRS. The results of the analysis provided a better of understandings on the MuRS capabilities, which are listed below:

- The Monte Carlo simulation indicates that the best cut that can be applied to the MuRS data, maintaining its current scintillator planes setup, is to identify as a pion any particle that stops at the fourth layer, while considering a muon any particle that traverses the last layer of scintillator planes. Such cut would provide a highly pure sample, with ∼99.6%, nevertheless, it will only be capable of identifying ∼8% of the pions within the range of $0.1 < p_\pi < 1$ GeV/c. Given the current 3% level uncertainty in the pion-argon cross-section measurement, such efficiency should yield a very small, if not ineffective, improvement in the final uncertainty.

- For the hypothetical situation where the full length of the detector is used (i.e. a scintillator plane is installed in the last layer of the detector), those numbers improve to ∼ 99.5% of purity and ∼10% of efficiency.

- The results of the simulation suggests that the iron structure might be shorter than the desired for its purpose.

The inconsistencies between the theoretical predictions presented in section 4.2.4 and the values given by the simulation could arise from 3 main origins: *i)* the simplicity of the theoretical predictions; *ii)* the difference between the density of pure iron and the real material used in the detector or; *iii)* errors in the Geant4 geometry file that defines the detector, used by LArIAT and this simulation analysis. However, such files were investigated and no errors were found.

Appendix A

Neutrino Physics

A.1 The Beta Decay Problem

Radioactivity was discovered in 1896 by Henri Becquerel and, in 1899, Ernest Rutherford classified radioactivity emissions into two types: α and β. In this context, the beta decay was considered to be a two-body decay. A β two-body decay consists of a nucleus A becoming a lighter nucleus B, with the emission of an electron, like the following

$$A \longrightarrow B + e^{-}, \tag{A.1}$$

resulting in the fact that the outgoing energies of the particles are kinematically determined. Using conservation of energy and momentum, it is easy to show that this energy is:

$$E = \frac{m_A^2 - m_B^2 + m_e^2}{2m_A} c^2. \tag{A.2}$$

As experiments conducted by Lise Meitner and Otto Han in 1911 showed, the electron energy spectrum was not well-defined as it was expected if the beta decay was a two-body decay. The electron energy spectrum was continuous, having as the maximum energy the one found on equation A.2 (see figure A.1) [41].

In 1930, Wolfgang Pauli proposed that the beta decay was not a two-body decay, but a three-body decay. The third particle proposed by him would be neutral and light. Pauli named it neutron. Later, with Chadwick's discovery of the neutron, Fermi proposed the change in the name of Pauli's particle to neutrino [41]. In 1933, Pauli and Perrin proposed that neutrinos were massless [41].

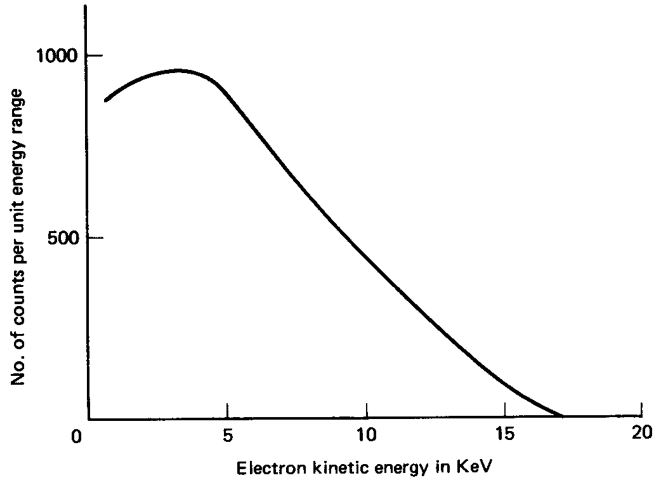

Figure A.1 | The beta decay spectrum of tritium
The figure shows the electron energy spectrum in a beta decay of tritium [41].

A.2 The First Neutrino Measurement

Neutrinos stayed without an experimental verification until 1956, when Cowan and Reines conducted an experiment at the Savannah River nuclear reactor in South Carolina. The experiment consisted basically of a big tank of water and cadmium chloride, surrounded by 4,200 litters of liquid scintillator, seating nearby the reactor. If neutrinos were real, the neutrinos produced by the nuclear reaction inside the reactor would hit the protons of the water and would produce a positron and a neutron. This reaction is called inverse beta decay and its equation is

$$\overline{\nu} + p^{+} \longrightarrow n + e^{+}. \tag{A.3}$$

The signals they were looking for were two photons produced by the electron-positron annihilation and a few photons produced by the neutron capture by the cadmium, a few micro-seconds after the positron signal [42]. They measured the signals they expected and published the results in a paper called “Detection of the Free Neutrino: A Confirmation” (Ref. [43]).

A.3 Different Types of Neutrinos

In 1953, Konopinski and Mahmoud proposed a rule to explain why certain reactions happen and some others do not. They did that by introducing a so called conservation of leptonic number rule. It was established that leptons would have a leptonic number L = 1, that antileptons would have leptonic number L = -1, and that any other particle would have leptonic number L = 0. By this rule an antineutrino should be produced in a beta decay. Although the rule explained the non-observation of many reactions, it did not covered all the cases. This led them to conclude that there was a leptonic number for each of the leptons. That is, a muonic number, an electronic number and, years later, a tauonic number (see table A.1) [44].

	Lepton number	**Electron number**	**Muon number**
Leptons			
e^-	1	1	0
ν_e	1	1	0
μ^-	1	0	1
ν_μ	1	0	1
Antileptons			
e^+	-1	-1	0
$\overline{\nu_e}$	-1	-1	0
μ^-	-1	0	-1
ν_μ	-1	0	-1

Table A.1 | The lepton family from 1962 to 1976 [41]

This hypothesis was experimentally checked in 1962 at the Brookhaven Nacional Laboratory by Lederman, Schwartz e Steinberger. The experiment they proposed consisted in observing the interaction of neutrinos produced in the pion decay with their detector. The source of pions was a charged pion beam in a particle accelerator called Alternating Gradient Synchrotron (AGS). The charged pion decays in a charged muon and its neutrino/antineutrino. In theory, if the leptonic number is the same for muons and electrons, the following reactions may occur:

$$\nu + n \longrightarrow p + e^- \tag{A.4}$$

$$\overline{\nu} + p \longrightarrow n + e^+ \tag{A.5}$$

$$\nu + n \longrightarrow p + \mu^- \tag{A.6}$$

$$\overline{\nu} + p \longrightarrow n + \mu^+ \tag{A.7}$$

In the experiment only the third and fourth reactions were observed, implying that the interaction of neutrinos produced with a muon can only produce other muons. That is, each lepton has a corresponding neutrino [45].

A.4 The Solar Neutrinos Flux Problem

The series of nuclear reactions occurring in the solar and stellar cores are given by the so-called carbon–nitrogen–oxygen (CNO) cycle and the pp-chain. In the CNO cycle the four protons are successively absorbed in a series of nuclei, starting and ending with carbon. In the pp-chain two protons combine to form the deuteron and further protons are added [46]. In either case, the net process is:

$$p + p + p + p \longrightarrow He^4 + e^+ + e^+ + \nu_e + \nu_e \qquad \text{(A.8)}$$

Ray Davis proposed an experiment to measure the neutrinos emitted by the sun. The experiment was based on the following inverse beta decay.

$$\nu_e + Cl^{37} \longrightarrow e^- + Ar^{37} \qquad \text{(A.9)}$$

The main idea is that the chlorine would absorb a solar neutrino and would produce an electron and an Ar^{37}. A tank containing 615 tons of a fluid rich in chlorine called tetrachloroethylene was placed in the Homestake gold mine in South Dakota. The fluid was periodically purged with Helium gas to remove the argon-37 atoms which were then counted by means of their radioactivity. In the average, the experiment measured one neutrino after every three days and ran for 30 years. Although the measurement of solar neutrinos was a success, the experiment measured a flux 2/3 smaller than the one theoretically predicted by John Bahcall. This difference became known as the solar neutrino problem and the results were published in 1970 [46].

A.5 Neutrino Oscillation

In 1967 Bruno Pontecorvo published a paper called “Neutrino Experiments and The Problem of Conservation of Leptonic Charge” in which he discussed the effect of neutrino oscillations for the solar neutrinos. He wrote [47]:

> *“From an observational point of view the ideal object is the sun. If the oscillation length is smaller than the radius of the sun region effectively producing neutrinos, direct oscillations will be smeared out and unobservable. The only effect on the earth’s surface would be that the flux of observable sun neutrinos must be two times smaller than the total (active and sterile) neutrino flux.”*

Thus, Pontecorvo anticipated the solar neutrino problem!

The next paper about neutrino oscillations was published two years later by V. Gribov and B. Pontecorvo. They considered a scheme of neutrino mixing and oscillations with four neutrino and antineutrino states: two left-handed states of neutrinos, ν_e and ν_μ, and two right-handed states of antineutrinos, $\overline{\nu}_e$ and $\overline{\nu}_\mu$. The main assumption of Gribov and Pontecorvo was that there are no sterile neutrino states [48].

A.5.1 Neutrino Oscillation Model

The current model of oscillations considers three neutrinos: The electron neutrino, the muon neutrino and the tau[1]

In this model, a neutrino flavor eigenstate with momentum $\vec{p}$ can be written as a linear combination of the neutrino mass eigenstates:

$$|\nu_\alpha\rangle = \sum_{k=1}^{n} U^*_{\alpha k} |\nu_k\rangle, \tag{A.10}$$

Where $\alpha = e, \mu, \tau$; $|\nu_k\rangle$ is the mass base, k is the known mass states and U is the Pontecorvo-Maki-Nakagawa-Sakata (PMNS) matrix [50, 51], that is:

$$U = \begin{pmatrix} 1 & 0 & 0 \\ 0 & c_{23} & s_{23} \\ 0 & -s_{23} & c_{23} \end{pmatrix} \begin{pmatrix} c_{13} & 0 & s_{13}e^{-i\delta} \\ 0 & 1 & 0 \\ -s_{13}e^{+i\delta} & 0 & c_{13} \end{pmatrix} \begin{pmatrix} c_{12} & s_{12} & 0 \\ -s_{12} & c_{12} & 0 \\ 0 & 0 & 1 \end{pmatrix} \tag{A.11}$$

where $c_{ij} \equiv \cos(\theta_{ij})$, $s_{ij} \equiv \operatorname{sen}(\theta_{ij})$ and δ is the Charge Parity (CP) symmetry violating phase parameter. In equation A.11, the three matrices represent different neutrino oscillation sectors. The left matrix represents the accelerator neutrino sector, the middle matrix represents the transition $\nu_e \to \nu_\tau$, that is present in both accelerator and reactor neutrino sectors, and the right matrix represents the reactor neutrino sector.

Consider that the flavor eigenstates are orthogonal, that the mass eigenstates are also orthogonal, that the PMNS matrix is unitary, that the neutrinos are oscillating in the vacuum, and also that the mass eigenstates are hamiltonian's eigenstates. The last statement leads to:

$$H|\nu_k\rangle = E_k|\nu_k\rangle \tag{A.12}$$

That means that the energy eigenvalues are

$$E_k = \sqrt{\vec{p}^2 + m_k^2}. \tag{A.13}$$

If we evolve the mass eigenstate in time, it is possible to write the flavor eigenstate as

$$|\nu_\alpha(t)\rangle = \sum_{k=1}^{n} U^*_{\alpha k} e^{-iE_k t} |\nu_k\rangle. \tag{A.14}$$

---

[1] The tau neutrino particle was detected in 1997 by The Direct Observation of NU Tau (DONuT) experiment at Fermilab [49].

Rewriting equation A.14 only in the flavor base yields

$$|\nu_\alpha(t)\rangle = \sum_{\beta=e,\mu,\tau} \left(\sum_{k=1}^{n} U^*_{\alpha k} U_{\beta k} e^{-iE_k t} \right) |\nu_\beta\rangle. \tag{A.15}$$

The term between parenthesis is the $\nu_\alpha \to \nu_\beta$ transition amplitude. With that information and some more algebra it is possible to show that the time dependent transition probability is

$$P_{\nu_\alpha \to \nu_\beta}(t) = \sum_{k=1}^{n} \sum_{j=1}^{n} U^*_{\alpha k} U_{\beta k} U_{\alpha j} U^*_{\beta j} e^{i(E_k - E_j)t}. \tag{A.16}$$

Some approximations and simplifications are possible. As neutrino masses are extremely small, they are in a relativistic regime. This allow the approximation, through Taylor expansion

$$E_k - E_j \approx \frac{m_k^2 - m_j^2}{2E} = \frac{\Delta m^2_{kj}}{2E}. \tag{A.17}$$

As neutrino's velocity is close to the light's one in vaccum

$$L \approx ct = t. \tag{A.18}$$

Separating the exponential in the equation A.16 into real and imaginary parts, the indexes in $k = j$ and $k > j$, and using some more algebra the final result is

$$\begin{aligned} P_{\nu_\alpha \to \nu_\beta}(L/E) &= \delta_{\alpha\beta} - 4 \sum_{k>j}^{n} \mathfrak{Re}[U^*_{\alpha k} U_{\beta k} U_{\alpha j} U^*_{\beta j}] \operatorname{sen}^2 \left(\frac{\Delta m^2_{kj} L}{4E} \right) \\ &\quad + 2 \sum_{k>j}^{n} \mathfrak{Im}[U^*_{\alpha k} U_{\beta k} U_{\alpha j} U^*_{\beta j}] \operatorname{sen} \left(\frac{\Delta m^2_{kj} L}{2E} \right). \end{aligned} \tag{A.19}$$

For the antineutrinos, the mathematical steps are similar [52].

First Neutrino Oscillation Measurements

The first oscillation measurements, and consequently the confirmation that neutrinos have mass, were made by the Super-Kamiokande experiment. The Super-Kamiokande detector is located 1 km underground in the Kamioka-mine, Hida-city, Gifu, Japan. It consists of a stainless-steel tank, with 39.3 m of diameter and 41.4 m tall, filled with 50,000 tons of ultra pure water. It has about of 13,000 photo-multipliers installed on the tank's wall (see image A.2). In 1998 the Super-Kamiokande collaboration published the first neutrino oscillation measurements in a paper called "Evidence for oscillation of atmospheric neutrinos" [53].

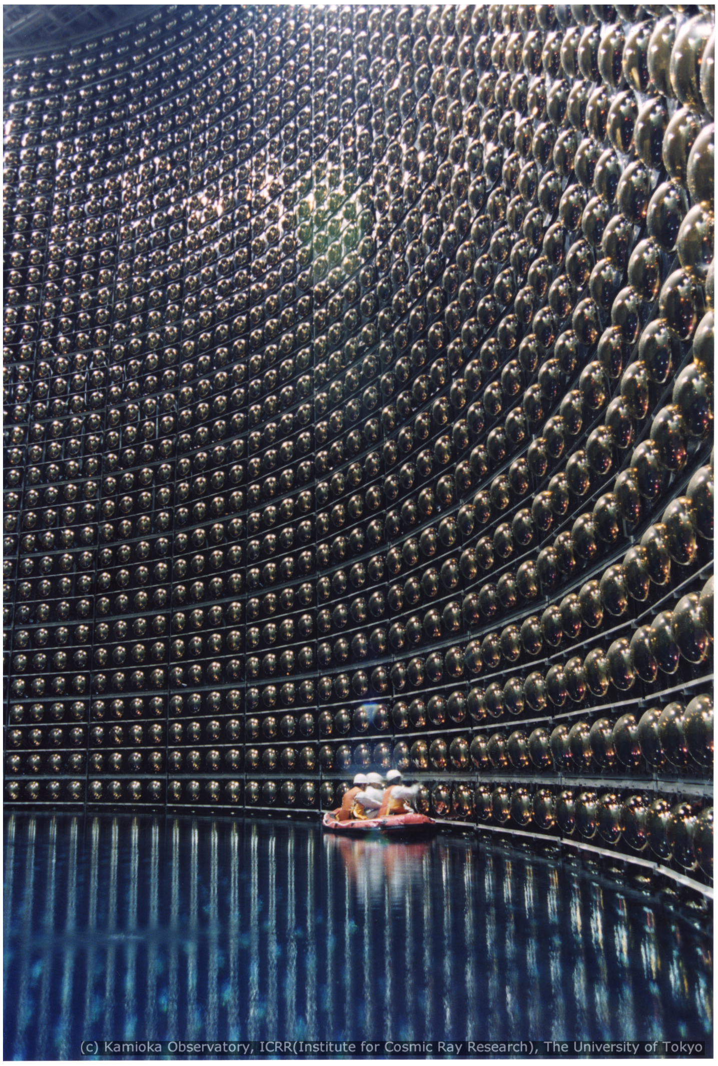

Figure A.2 | Inside Super-Kamiokande tank
Workers doing photomultipliers (PMTs) checking inside Super-Kamiokande detector [54].

The CP Symmetry Violating Phase Parameter

The δ parameter showed in the PMNS matrix in equation A.11 quantifies the charge conjugation and parity symmetry violation phase. The strong and electromagnetic interactions are invariant under CP symmetry, but some weak interaction processes are not. This violating phase parameter is also observed in the quark sector and was already measured. The CP symmetry violating phase parameter is still not observed in the leptonic sector.

The Character of the Neutrino Mass Spectrum (Mass Hierarchy)

The equation A.19 limits that the data of neutrino oscillation experiments can only measure the mass-squared differences. Due to the tremendous growth of the neutrino experiment efforts in the past two decades, it is known that [55]

$$\Delta m^2_{21} = (7.53 \pm 0.18) \times 10^{-5}\,\mathrm{eV}^2 \tag{A.20}$$

and [56]

$$\Delta m^2_{32} = (2.34 \pm 0.09) \times 10^{-3}\,\mathrm{eV}^2 \tag{A.21}$$

or

$$\Delta m^2_{32} = (-2.37^{+0.07}_{-0.11}) \times 10^{-3}\,\mathrm{eV}^2. \tag{A.22}$$

The relative ordering $m_1 < m_2$ is known through observations of solar neutrinos, which are subject to resonant matter effects in the sun [55]. The value in A.21 corresponds to what is called Normal Hierarchy and A.22 to what is called Inverted Hierarchy. Normal hierarchy is the condition where the $m_1 < m_2 < m_3$. Inverted hierarchy is the condition where the $m_3 < m_1 < m_2$. A schematic of the normal and inverted hierarchies can be found on figure A.3. The precision of neutrino sector measurements has reached a point where the unknown hierarchy is a major hurdle to further progress [57].

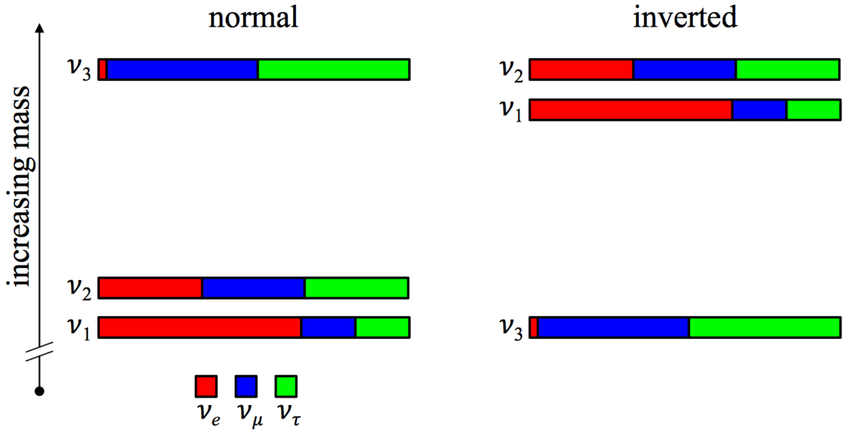

Figure A.3 | The Mass Hierarchy
The two possible neutrino mass hierarchies. The colors represent the approximate flavor admixtures present in each mass eigenstate [57].

The θ_{23} Octant Definition Problem

The θ_{23} parameter is present is both $P_{\nu_\mu \to \nu_\mu}$ and $P_{\nu_\mu \to \nu_e}$ calculations. Most of the near past neutrino experiments take advantage of an approximation that considers the existence of only two neutrino flavors due to limitations in their resolution. In this approximation the oscillation probabilities take the form of

$$P_{\nu_\mu \to \nu_e} \propto \sin^2(2\theta_{23}) \text{ and } P_{\nu_\mu \to \nu_\mu} \propto \sin^2(2\theta_{23}),$$

which implies in a redundancy in the value of θ_{23}, with the possibilities being either $\theta_{23} > \pi/4$ or $\theta_{23} < \pi/4$. In more recent results, experiments such as NuMI Off-axis ν_e Appearance (NOνA), Main Injector Neutrino Oscillation (MINOS) and Tokai to Kamioka (T2K), do not use this approximation, resulting in a 2 fold degeneracy solution for the mixing angle θ_{23}. The latest results were presented by the NOνA Collaboration and can be seen in figure A.4, which shows the two best fit values with their 90% confidence level contours. In this study, NOνA Collaboration disfavored the maximal mixing ($sin^2\theta_{23} = 0.5$) scenario with 2.6σ significance [58].

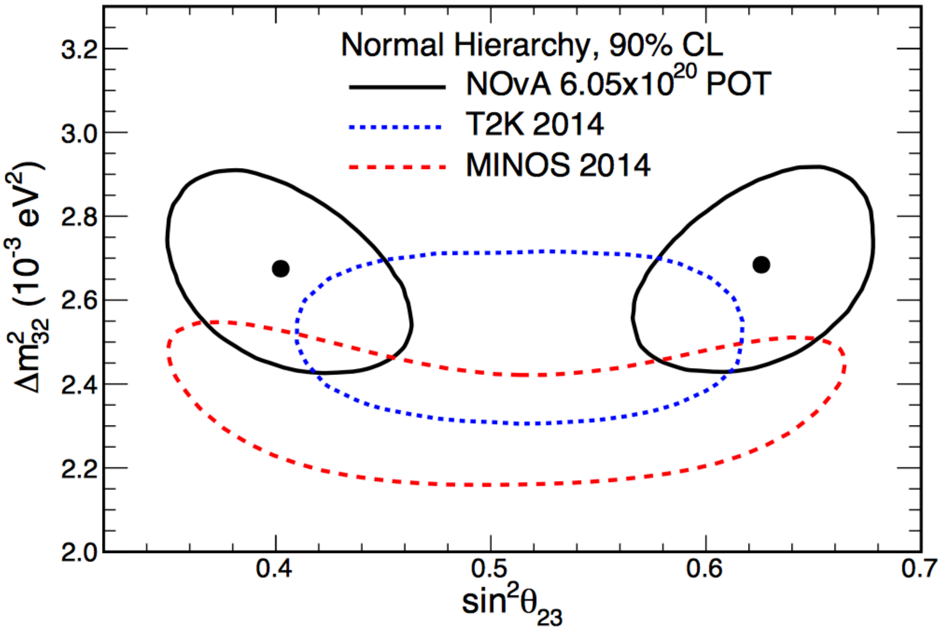

Figure A.4 | Preliminary θ_{23} results from the NOνA Experiment
Best fit (black dots) and allowed 90% confidence level regions (solid black curves) of $\sin^2\theta_{23}$ and Δm^2_{32} for the normal hierarchy. The dashed curves show MINOS [59] and T2K [60] 90% confidence level contours [58].

Appendix B

Negative Pion Cross Section Review

Total pion-nucleus cross-sections can be divided into mainly 4 channels: *i)* elastic scattering, *ii)* inclusive inelastic scattering, *iii)* true absorption, and *iv)* single charge exchange, all depending on the charge and energy of the incoming pion. The definition of each of these channels is described as follow:

1. **Elastic scattering:** In the elastic scattering the kinetic energy of the particle in the center of mass frame is conserved after the interaction, while its direction is deflected.
2. **Inelastic scattering:** In this type of scattering interaction the energy of the particle in the center of mass frame is not conserved, since there is an exchange of energy between the interacting particles.
3. **True absorption:** In this case, the interaction of the colliding particle results in its total absorption by one of the nuclei of the target material.
4. **Single charge exchange:** As the name suggest, the interaction between the incident particle and a nucleus of a said material results in a unit of charge exchange between the particle and one of its nucleons. An example of such case is the interaction $\pi^+ n \rightarrow p\pi^0$.

Since the late 1950s only a handful of experiments measured the inclusive negative pion cross-section within LArIAT's operational momentum range (from 0.2 GeV/c to 2.0 GeV/c), which will be briefly revised in this Chapter.

B.1 The results from the Center of Nuclear Studies at Saclair [61]

This study was published by J. C. Brisson *et al.* in 1959, at the Nuclear Studies at Saclair, France, reporting total cross-section measurements at a range of 0.4 to 1.2 GeV. This result uses a proton synchrotron and a carbon target to produce a pion beam with variable energy. Said beam is then focused to a liquid hydrogen target, whose throughgoing particles are detected by a counter telescope. The results provide information on $\sigma(E)$, as shown in figure B.1.

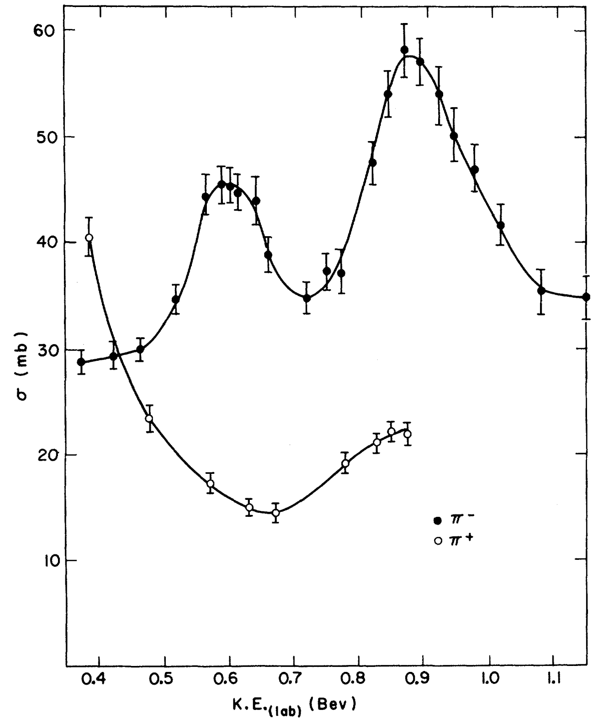

Figure B.1 | Plot shows the experimental total cross-section results for $\pi^{\pm}$ with a proton target, as a function of energy. The two maxima at ~570 MeV and ~880 MeV represent two pion-nucleon resonance states [61].

The data was collected using only one target type and, thus, cannot be used as a mean to extrapolate the pion cross-section to other targets, such as Argon.

B.2 The results from Berkeley [62]

This study was carried forward by producing a negative pion beam using Berkeley's internal proton synchrotron and a beryllium target. The time coincidence from three plastic scintillators, depicted by number 1, 2, and 3 in figure B.2, were used in order to provide a total inclusive cross-section measurement. The first couple of scintillators were placed prior to the target, whilst the last one took data at different distances from the target, yielding results for different solid angles. Measurements of the total attenuation of the pion beam were performed for five different energy values (all in MeV): 230, 290, 370, 427, and 460.

The total apparent pion cross-section is given by the difference between the pion total attenuation measurements and the calculated Coulomb-scattering cross-section, in order to remove the electromagnetic interaction effect. The final results are compiled in figure B.3, which shows the final total pion cross-sections for each of the six different energy beams used, along with the

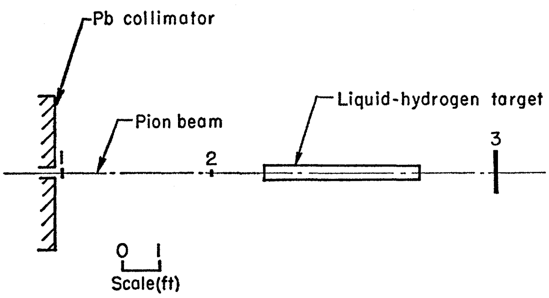

Figure B.2 | Schematic view of the experimental apparatus used by the team at Berkeley. Numbers 1, 2, and 3 represent the three plastic scintillators used in the study, with the 3rd one being moved to provide measurements at different solid angles [62].

fitted curves for each case. The fitting function follows the form

$$\sigma(\Omega) = A + B(\Omega)^2, \tag{B.1}$$

which was chosen in order to provide a zero slope at $\Omega = 0$.

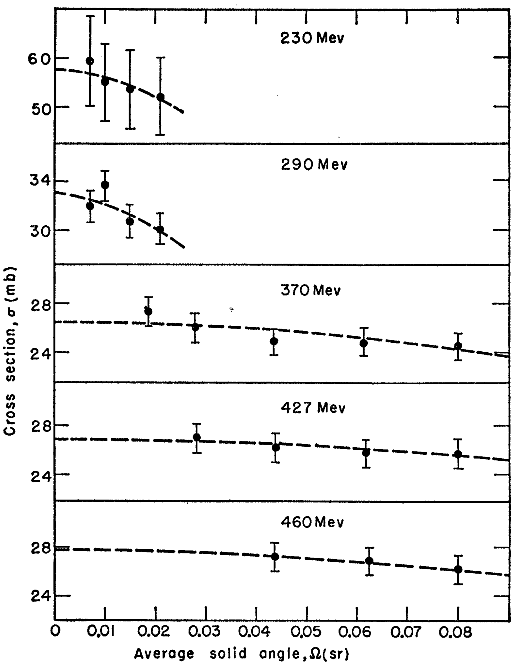

Figure B.3 | The experimental results for the total $\pi^- p$ cross-section for different beam energies and different solid angles. The dashed curves represent the best fit using equation B.1 [62].

The results provide useful information of $\sigma(\Omega)$, but, similarly to the previous section, it cannot be used as a starting point to extrapolate a possible π-Ar cross-section.

B.3 The results from Swiss Institute for Nuclear Research (SIN) [63, 64]

On the apparatus

The SIN performed two different measurements, in 1981 and 1983, with both studies using two different setups of the same apparatus, which were named as the scattering experiment and the transmission experiment.

The pion beam was set to operate in six different energy configurations for positive pions and two energy values for the negative ones: 125 and 165 MeV. The beam was pointed to targets of Li, C, Al, Fe, Nb, and Bi with densities of 0.59, 1.88, 2.28, 2.53, 4.36, and 4.69 g/cm^2 respectively. In order to monitor the beam flux, 3 plastic scintillators were placed before the target, with the last one having a hole of 5×5 cm^2, used to fit different target materials in it. The data was monitored in coincidence with the 2 first scintillator paddles plus an anti coincidence with the last one in order to guarantee that all the selected data was traversing the fitted target.

For the transmission experiment, downstream the target position, five plastic scintillators were displaced in such a way to cover a solid-angle range of 0.1-0.7 sr. These plastic scintillator counters were build in a fashion that allowed them to be moved longitudinally with respect to the target. Changing the distance between the counters and the target enabled taking data for different solid-angles. As such, 9 different solid-angle measurements were performed for four of the aforementioned targets (namely Li, C, Al, and Fe), while the last two (Nb and Bi) included data from 13 different solid angles. The counters before and after the target allow the measurement of the beam flux and, consequently, the number of pions absorbed by each target. A schematic of this setup can be seen in figure B.4 (a). This experiment provided the measurements for charge exchange and true absorption components, according to equation B.2

$$\sigma_{\text{tr}}(\Omega) = \frac{1}{n_t} \ln\left(\frac{N(0)}{N(t)}\right) = \sigma_{\text{abs}} + \sigma_{\text{cx}} + \int_{\Omega}^{4\pi} \frac{d\sigma_{\text{sc}}}{d\Omega} d\Omega, \tag{B.2}$$

where σ_{tr} is the transmission cross-section, Ω is the solid angle, n_t is the number of nuclei in the target, $N(0)$ and $N(t)$ are the number of counts with and without a target in the beam line, σ_{abs} is the true absorption cross-section, σ_{cx} is the charge exchange cross-section term and, finally, σ_{sc} is the contribution from both inelastic and elastic scatterings.

The scattering experiment provided measurements on the differential scattering cross-section component (the last term on equation B.2). The experimental apparatus used was kept similar to the previous one, except for the instruments located after the target. In this case, the outgoing pions were measured by three telescopes, each consisting of two cubes of 5×5×5 cm^3 of plastic scintillator, placed at a distance of 55 cm from the center of the target, and separated by 10°. A schematic of this experimental setup can be seen in figure B.4 (b).

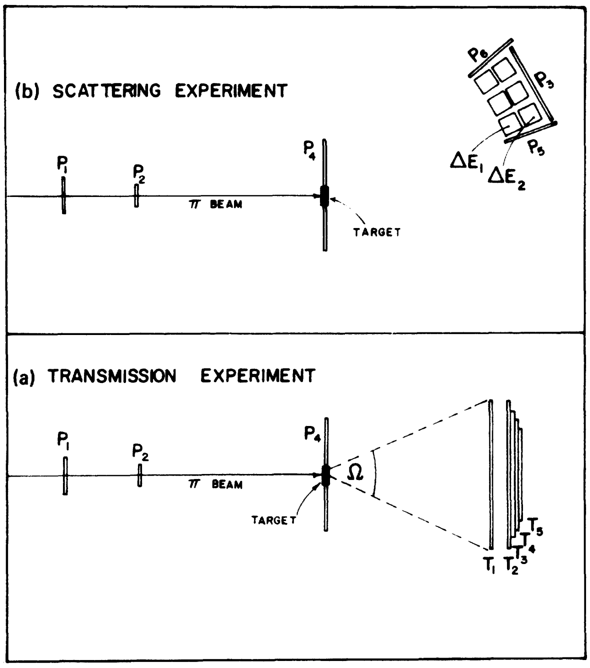

Figure B.4 | Schematic view of the experimental apparatus used by the SIN experiments [63].

On the results

The inelastic component was obtained by subtracting the measured elastic scattering, absorption, and charge exchange cross sections from the total cross section term, the latter being a result provided by a previous experiment [65]. As such, the inelastic component is written as

$$\sigma_{inel} = \sigma_{tot} - \sigma_{el} - \big(\sigma_{abs} + \sigma_{cx}\big). \tag{B.3}$$

For the true absorption and charge exchange measurements, since the contribution of the charge exchange for the total measurement is small (around $\sim$15%), a crude estimation of it is already enough to allow for a good approximation on the calculation of the true absorption (with errors up to 20%). Thus, for this result, the true absorption component was calculated based on the estimation of the charge exchange cross-section term. The results of the calculations, measurements (from both this and previous experiment), and estimations can be seen on table B.1.

π^- experimental cross-section results

E_π	Nucleon	N_{eff}	$\sigma_{\text{abs}} + \sigma_{\text{cx}}$	σ_{cx}	σ_{abs}	σ_{tot}	σ_{el}	σ_{inel}
(MeV)	–	(mb)	(mb)	(mb)	(mb)	(mb)	(mb)	(mb)
125	Li	1.85	154 ± 18	37 ± 15	117 ± 22	500 ± 9	161 ± 16	185 ± 26
	C	1.86	253 ± 24	46 ± 20	207 ± 30	673 ± 14	244 ± 24	176 ± 37
	Al	2.48	464 ± 39	50 ± 25	414 ± 46	1134 ± 40	465 ± 47	205 ± 73
	Fe	3.56	728 ± 61	80 ± 40	648 ± 70	1948 ± 80	822 ± 82	398 ± 130
	Nb	4.51	1035 ± 93	100 ± 50	935 ± 100	2735 ± 200	1190 ± 240	510 ± 330
	Bi	7.1	1450 ± 300	138 ± 70	1312 ± 310	5088 ± 400	2140 ± 430	1498 ± 660
165	Li	1.41	160 ± 34	39 ± 16	121 ± 37	556 ± 9	159 ± 16	237 ± 40
	C	1.27	249 ± 26	45 ± 20	204 ± 33	684 ± 9	242 ± 24	193 ± 37
	Al	1.69	449 ± 47	50 ± 25	399 ± 70	1122 ± 40	466 ± 47	207 ± 78
	Fe	2.43	741 ± 73	70 ± 35	671 ± 80	1868 ± 80	823 ± 82	304 ± 136
	Nb	3.13	864 ± 80	120 ± 60	744 ± 100	2725 ± 170	1186 ± 240	675 ± 300
	Bi	5.26	1220 ± 250	170 ± 85	1050 ± 265	4904 ± 300	2107 ± 420	1577 ± 570
50	C	–	238 ± 24	18	220 ± 30	–	–	–
	Fe	–	1232 ± 92	35	1197 ± 102	–	–	–
	Bi	–	5137 ± 328	49	5088 ± 343	–	–	–

Table B.1 | The table shows the different cross-section terms for 3 available energies of π^- beams interacting with different natural targets.

The measurement presented on the 1983 paper [65] had fewer data points. For that measurement, only a term accounting for both absorption and charge exchange was obtained. Each individual term was then computed by estimating the charge exchange component and calculating the absorption term by subtracting said estimation from the total measure.

Extrapolating the data to π^--Ar

Using the data of the total cross-section term for both 125 and 165 MeV energies extracted from the experimental results shown in table B.1, it is possible to plot the total cross-section as a function of the atomic number, as it is shown in figure B.5. A fit following the function

$$\sigma_{\text{tot}} = AZ^B, \tag{B.4}$$

where Z is the atomic number, and A and B are the fitting terms applied to the data points (solid red line) in order to provide an extrapolation for the total cross-section of π^--Ar, which is indicated by the blue star.

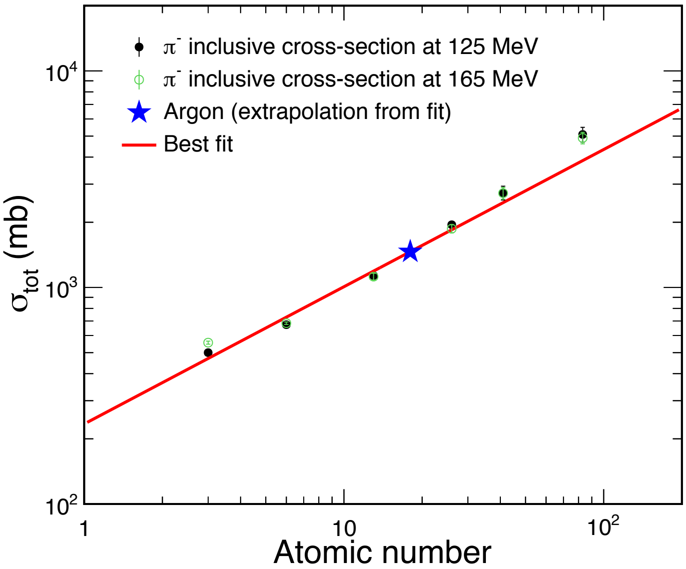

Figure B.5 | Plot of the total cross-section term as a function of atomic number for the data presented in table B.1. The solid red line indicates the best fit, and the blue star indicates the expected total cross-section for π^--Ar from the fitting parameters.

Appendix C

LArIAT's Cross Section Measurement Method and First Results

C.1 LArIAT's Cross Section Measurement Method and First Results

C.1.1 Cross section measurements

Consider that the LArIAT TPC is divided in many thin slices, such as in figure C.1.

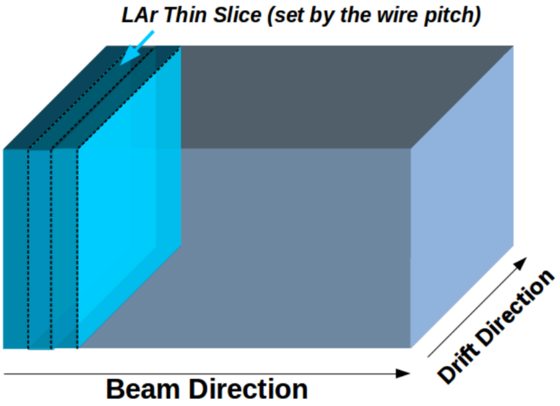

Figure C.1 | LArIAT TPC sliced
Representation of how the TPC is sliced to calculate the particles cross section [34].

For each slice the number of incident particles ($N_{incident}$) and the number of particles that interacted ($N_{interacting}$) are measured (see figure C.2).

The probability of interaction ($P_{interacting}$) is defined as

$$P_{interacting} = \frac{N_{interacting}}{N_{incident}}, \tag{C.1}$$

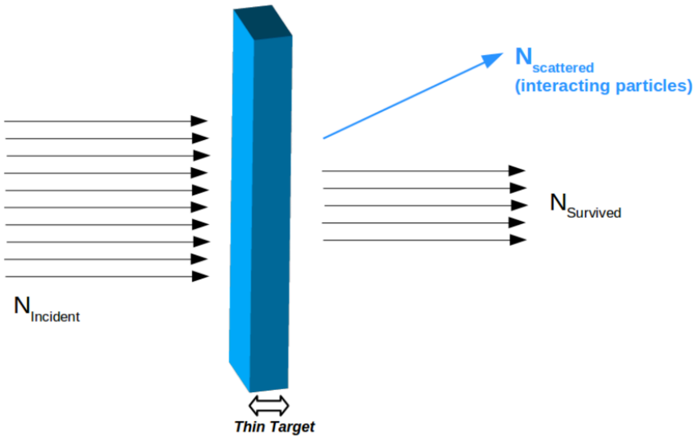

Figure C.2 | LArIAT TPC slice
Representation of a slice of the LArIAT TPC and the number of incident, interacting and survival particles [34].

which is correlated to the total cross section by [32]

$$P_{interacting} = 1 - P_{survival} = 1 - e^{-\sigma_{total} n \delta x}, \tag{C.2}$$

where σ_{total} is the total cross section, n is the density of scattering centers and δx is the thickness of the slice. As the thickness of the slice is small, we can Taylor expand the equation C.2 and solve for the cross section:

$$P_{interacting} = 1 - e^{-\sigma_{total} n \delta x} = 1 - (1 - \sigma_{total} n \delta x + ...). \tag{C.3}$$

Using equation C.3 and the value of the interaction probability (that is measured using the relation C.1), the total cross section as a function of the kinetic energy is given by

$$\sigma_{total}(KE) \sim \frac{1}{n\delta x} \frac{N_{interacting}}{N_{incident}}. \tag{C.4}$$

As LArTPCs are extremely granular, it is considered that the wire-by-wire spacing is the thickness of the slice, and it is known the incident energy at each slice. The wire-by-wire horizontal distance in LArIAT is of the order of 5 mm [34]. In LArIAT, the measurement of the cross section can be done by defining two histograms: i) the kinetic energy of the interacting particles and ii) the kinetic energy of the incident particles. In each slice, it is verified if the particle interacted or not, and its kinetic energy is calculated as follows

$$KE_{slice} = \sqrt{p^2 - m} - m - E_{flat} - \sum_{i=0}^{k-1} \left(\frac{dE}{dX}\right)_i \times \delta x_i, \tag{C.5}$$

where p is momentum reconstructed in the wire chambers, m is the mass obtained in the TOF detectors, E_{flat} is a constant that adjusts the energy by the energy loss that takes place in the face of cryostat material and k is the number of slices. In case the particle has interacted, this entry is added to the interacting histogram, otherwise, the entry is added to the incident histogram. Finally, following equation C.4, the cross section, as a function of energy can be found by dividing the interacting histogram by the incident histogram.

This method can only be applied if a particle track is selected, and the mass and the point of interaction can be identified. In order to have all the needed information, some cuts are applied on the candidates. The selection has three steps:

- A particle identification is required from the TOF detectors.
- A clean match is required between the extrapolated trajectory of the identified particle in the two last set of wire chambers and the start of a track in the front TPC (see figure C.3).
- In order to remove electrons from the selected sample, the identified TPC track is examined and vetoed if it displays the profile of an electromagnetic shower [34].

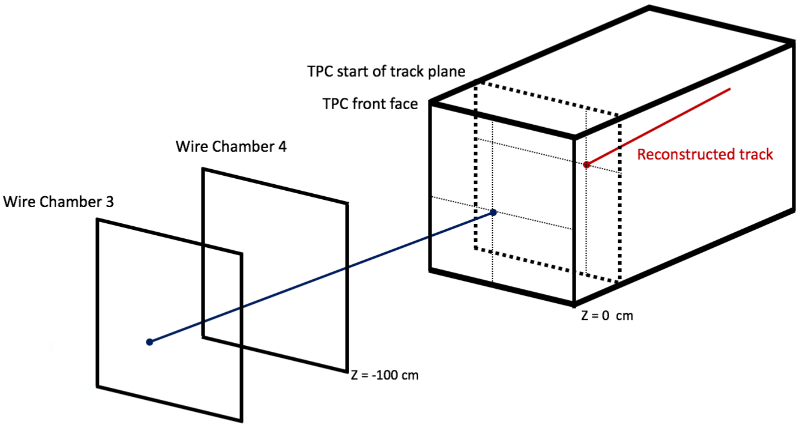

Figure C.3 | Clean match between wire chamber and TPC requirement
The figure illustrates the clean match requirement between the wire chambers' information and the TPC for reconstructed tracks.

The choice of the momentum range

C.1.2 LArIAT's first π^-–argon cross section measurement

Assembling the first run data and using the method described above, LArIAT produced the first π^-– argon cross section measurement, that can be seen in figure C.4.

The preliminary systematic uncertainties are:

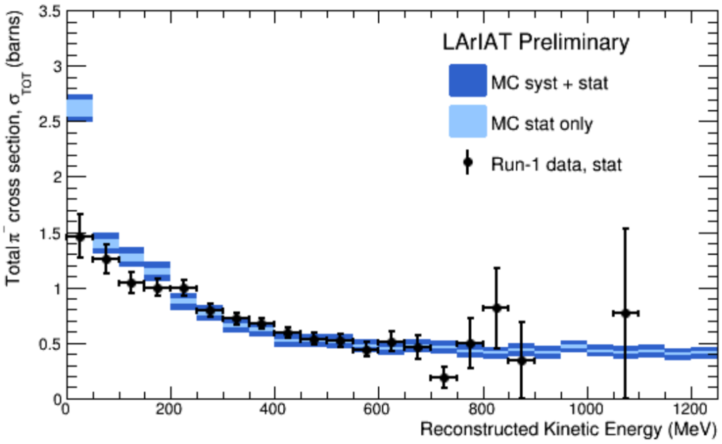

Figure C.4 | LArIAT's first π^-– argon cross section measured
LArIAT's first π^-– argon cross section measured. This result was produced only with data collected on the first run [34].

Source of systematic uncertainty	Uncertainty
$\frac{dE}{dX}$ calibration	5%
E_{flat}	3%
Contamination from through-going muons	3%
Reconstructed momentum from the wire chambers	3%

Table C.1 | LArIAT systematic uncertainties [34]

Bibliography

[1] D. R. Nygren, **The Time Projection Chamber: A New Detector for Charged Particles**. eConf, vol. C740805, p. 58, 1974.

[2] R. Acciarri (LArIAT Collaboration), **LArIAT: Liquid Argon In a Testbeam.** Internal report. DocDB-1975. 2016.

[3] C. Rubbia, **The Liquid Argon Time Projection Chamber: A New Concept for Neutrino Detectors**. CERN EP Internal Report 77-8. 1977.

[4] S. Amerio *et al.*, (ICARUS Collaboration), **Design, construction and tests of the ICARUS T600 detector**. Nucl. Instr. and Meth. in Phys. Res. **A 527**, 329. 2004.

[5] K. Mavrokoridis *et al.*, **Argon Purification Studies and a Novel Liquid Argon Recirculation System**. arXiv:1106.5226. 2011.

[6] A. Aguilar-Arevalo *et al.*, **The MiniBooNE Detector.** arXiv:0806.4201. 2008.

[7] **Booster Department**. Retrieved from http://www-ad.fnal.gov/proton/booster.html

[8] A. Aguilar-Arevalo *et al.*, **A Search for Electron Neutrino Appearance at the Delta m**2 1 eV**2 Scale.** Phys. Rev. Lett. **98**, 231801. 2007.

[9] C. Giunti and M. Laveder, ν_e **Disappearance in MiniBooNE**. arXiv:0707.4593. 2008

[10] H. Chen *et al.*, **A Proposal for a New Experiment Using the Booster and NuMI Neutrino Beamlines: MicroBooNE**. 2007.

[11] **About the Detector**. n.d. Retrieved from http://www-microboone.fnal.gov/public/aboutdetector.html

[12] M. Antonello *et al.*, **Precision measurement of the neutrino velocity with the ICARUS detector in the CNGS beam.** JHEP **11**, 049. 2012.

[13] M. Antonello *et al.*, **ICARUS at FNAL.** arXiv:1312.7252v2. 2014.

[14] R. Acciarri *et al.* **A Proposal for a Three Detector Short-Baseline Neutrino Oscillation Program in the Fermilab Booster Neutrino Beam.** arXiv:1503.01520v1. 2013.

[15] R. Acciarri *et al.*, **Long-Baseline Neutrino Facility (LBNF) and Deep Underground Neutrino Experiment (DUNE) Conceptual Design Report Volume 1: The LBNF and DUNE Projects**. arXiv:1601.05471. 2016.

[16] M. Anfreville *et al.*, **The Drift Chambers Of The NOMAD Experiment.** arXiv:hep-ex/0104012. 2001.

[17] J. Strait *et al.*, **Long-Baseline Neutrino Facility (LBNF) and Deep Underground Neutrino Experiment (DUNE) Conceptual Design Report Volume 3: Long-Baseline Neutrino Facility for DUNE June 24, 2015.** arXiv:1601.05823. 2016.

[18] J. Paley *et al.*, **LArIAT: Liquid Argon In A Testbeam.** arXiv:1406.5560. 2014.

[19] W. Foreman, **First Run of the LArIAT Testbeam Experiment.** arXiv:1511.00305. 2015.

[20] R. Acciarri (LArIAT Collaboration), **LArIAT: Liquid Argon In a Testbeam.** Internal report. DocDb-1975. 2016.

[21] C. Anderson *et al.*, **First Measurements of Inclusive Muon Neutrino Charged Current Differential Cross Sections on Argon**. Phys. Rev. Lett. **108**, 161802. 2012.

[22] L. Alvarez-Ruso *et al.*, **NuSTEC White Paper: Status and Challenges of Neutrino-Nucleus Scattering.** arXiv:1706.03621v2. 2017.

[23] A. Bueno *et al.*, **Nucleon Decay Searches with large Liquid Argon TPC Detectors at Shallow Depths: atmospheric neutrinos and cosmogenic backgrounds.** arXiv:hep-ph/0701101. 2007.

[24] R. Acciarri *et al.*, **A study of electron recombination using highly ionizing particles in the ArgoNeuT Liquid Argon TPC.** arXiv:1306.1712. 2013.

[25] S. Agostinelli *et al.* **Geant4 – a simulation toolkit**. Nuclear Instruments and Methods in Physics Research Section A **506**, 3, 250. 2003.

[26] J. Orwig, **Cockcroft-Walton's successor: a peep inside the new RFQ and how it works**. 2012. Retrieved from http://www.fnal.gov/pub/today/archive/archive_2012/today12-11-02_RFQReadmore.html

[27] **Fermilab Linac**. 2014. Retrieved from http://www-bd.fnal.gov/proton/linac.html/

[28] **Booster Department**. Retrieved from http://www-ad.fnal.gov/proton/booster.html

[29] S. Nagaitsev, **Fermilab Antiproton Source, Recycler Ring, and Main Injector**. arXiv:1408.0759. 2014.

[30] P. Adamson, *et al.* (MINOS Collaboration) **The NuMI neutrino beam**. Nucl. Instr. Meth. A **806**, 279-306. 2016.

[31] **MTest Beam Areas**. Retrieved from http://ftbf.fnal.gov/mtest-beam-areas/

[32] W. R. Leo, **Technics for nuclear and particle physics experiments**. Springer-Verlag. 1987.

[33] A. Pla-Dalmau, **Design of Fluorescent Compounds for Scintillation Detection**. Northern Illinois University. 1990.

[34] P. Hamilton, **LArIAT: Worlds First Pion-Argon Cross-Section**. arXiv:1611.00821. 2016.

[35] B. Soubasis (LArIAT Collaboration), **Aerogel Threshold Cherenkov Update in LArIAT**. Internal report. DocDB-1992. 2016.

[36] P. Eckert *et al.*, **Characterisation studies of silicon photomultipliers**. Nucl. Instrum. Methods **A 620**, 217–226. 2010.

[37] O. B. Rodrigues (LArIAT Collaboration), **Monte Carlo simulation of particles penetration depth in the LArIAT Muon Range Stack detector** Internal report. DocDB-3252. 2017.

[38] S. Agostinelli *et al.* **Geant4 – a simulation toolkit**. Nuclear Instruments and Methods in Physics Research Section A **506**, 3, 250. 2003.

[39] J. Allison *et al.* **Geant4 developments and applications**. IEEE Transactions on Nuclear Science **53**, No. 1, 270. 2006.

[40] J. Allison *et al.* **Recent developments in Geant4**. Nuclear Instruments and Methods in Physics Research A **835**, 1, 186. 2016.

[41] D. Griffiths, **Introduction to Elementary Particle Physics**. Second edition, Wiley-VCH Verlag GmbH & Co. KGaA, Weinheim. ISBN 978-3-527-40601-2. 2008.

[42] K. V. L. Sarma, **Nobel Leptons**. arXiv:hep-ph/9512420. 1995.

[43] C. L. Cowan, F. Reines, F. B. Harrison, H. W. Kruse, and A. D. McGuire. **Detection of the Free Neutrino: A Confirmation**. Science. 1956.

[44] E. J. Konopinski, H. M. Mahmoud, **The Universal Fermi Interaction**. Phys. Rev. **92**. 1953.

[45] G. Danby, J-M. Gaillard, K. Goulianos, L. M . Lederman, N. Mistry, M. Schwartz, J. Steinberger, **Observation of high-energy neutrino reactions and the existence of two kinds of neutrinos.** Phys. Rev. Lett. **9**, 1, 36. 1962.

[46] G. Rajasekaran, **The Story of the Neutrino**. arXiv:1606.08715. 2016.

[47] B. Pontecorvo, **Neutrino Experiments and The Problem of Conservation of Leptonic Charge**. Theoret. Phys. **53**, 1717 (1967), Sov. Phys. JETP **26**, 984. 1968.

[48] S. M. Bilenky, **Neutrino oscillations: brief history and present status**. arXiv:1408.2864. 2014.

[49] K. Kodama *et al.*, **Observation of tau neutrino interactions.** Phys. Lett. B **504**, 218-224. 2001.

[50] Z. Maki *et al.*, **Remarks on the Unified Model of Elementary Particles**. Prog. Theor. Phys. **28**, 870-880. 1962.

[51] B. Pontecorvo, **Inverse beta processes and nonconservation of lepton charge**. Soviet Phys. JETP. **7**, 172. 1958.

[52] C. Giunti, C. K. Kim, **Fundamentals of Neutrino Physics and Astrophysics**. Oxford University Press. ISBN 978-0-19-850871-7. 2007.

[53] Y. Fukuda *et al.*, **Evidence for oscillation of atmospheric neutrinos**. Phys. Rev. Lett. **81**, 1562. 1998.

[54] Workers doing PMTs checking during Super-Kamiokande's construction. Digital image. Super-Kamiokande collaboration, n.p. Web 17 May, 2010. 16 Jan 2017. http://www-sk.icrr.u-tokyo.ac.jp/sk/gallery/index-e.html

[55] A. Gando *et al.*, **Neutrino-nucleus quasi-elastic and 2p2h interactions up to 10 GeV**. Phys. Rev. D **88**, 033001. 2013.

[56] P. Adamson *et al.*, **Combined Analysis of ν_μ Disappearance and $\nu_\mu \to \nu_e$ Appearance in MINOS Using Accelerator and Atmospheric Neutrinos**. Phys. Rev. Lett. **112**, 191801 (2014); and update by A. Sousa for MINOS at XXVI International Conference on Neutrino Physics and Astrophysics (Neutrino 2014), proceedings at arXiv:1502.07715. 2015.

[57] R. B. Patterson, **Prospects for measurement of the neutrino mass hierarchy**. arXiv:1506.07917v3. 2016.

[58] P. Adamson *et al.*, **Measurement of the neutrino mixing angle θ_{23} in NOvA**. arXiv:1701.05891. 2017.

[59] P. Adamson *et al.*, **Combined Analysis of ν_μ Disappearance and $\nu_\mu \to \nu_e$ Appearance in MINOS Using Accelerator and Atmospheric Neutrinos**. Phys. Rev. Lett. **112**, 191801. 2014.

[60] K. Abe *et al.*, **Measurements of neutrino oscillation in appearance and disappearance channels by the T2K experiment with 6.6×10^{20} protons on target**. Phys. Rev. D **91**, 072010. 2015.

[61] J. C. Brisson, *et al.* **Measurements on the $\pi^{\pm}$p Total Scattering Cross Sections in the Energy Range of 0.4 to 1.5 Bev**. Phys. Rev. Lett. **3**, 561. 1959.

[62] J. C. Caris, *et al.* **Total Cross Sections for Negative Pions on Protons at 230, 290, 37O, 427, and 460 Mev**. Phys. Rev. **122**, Vol. 1, 262. 1961.

[63] D. Ashery *et al.* **True absorption and scattering of pions on nuclei**. Phys. Rev. C **23**, N. 5, 2173. 1981.

[64] D. Ashery *et al.* **True absorption and Scattering of 50 MeV pions**. Phys. Rev. C **28**, N. 6, 2548 (Rapid Communications). 1983.

[65] A. S. Carroll *et al.* **Pion-nucleus total cross sections in the (3,3) resonance region**. Phys. Rev. C **14**, N. 2, 635. 1976.